PFG

Photogrammetrie Fernerkundung Geoinformation

Journal for Photogrammetry, Remote Sensing and Geoinformation Science

Organ der Deutschen Gesellschaft für Photogrammetrie, Fernerkundung und Geoinformation (DGPF) e. V.

Jahrgang 2014, Heft 3

E. Schweizerbart'sche Verlagsbuchhandlung (Nägele u. Obermiller) Stuttgart 2014

Deutsche Gesellschaft für Photogrammetrie, Fernerkundung
und Geoinformation (DGPF) e. V.
Gegründet 1909

Die *Deutsche Gesellschaft für Photogrammetrie, Fernerkundung und Geoinformation* (DGPF) e. V. unterstützt als Mitglieds- bzw. Trägergesellschaft die folgenden Dachverbände:

International Society
for Photogrammetry
and Remote Sensing

DAGM

Deutsche Arbeits-
gemeinschaft für
Mustererkennung e.V.

GeoUnion
Alfred-Wegener-Stiftung

Herausgeber:

Präsident: Prof. Dr. Thomas Kolbe, Technische Universität München, Institut für Geodäsie, GIS und Landmanagement, Lehrstuhl für Geoinformatik, Arcisstraße 21, 80333 München, Germany, Tel. +49-89-289-23888
Geschäftsstelle: Tanja Nyc, c/o Technische Universität München, Institut für Geodäsie, GIS und Landmanagement, Lehrstuhl für Geoinformatik, Arcisstraße 21, 80333 München, Germany, Tel.: +49-89-289-22578, e-mail: geschaeftsstelle@dgpf.de, Gläubiger-Identifikationsnummer DE54 ZZZ0 0000 8351 37
Published by: E. Schweizerbart'sche Verlagsbuchhandlung (Nägele u. Obermiller), Johannesstraße 3A, 70176 Stuttgart, Germany, Tel.: +49-711 351456-0, Fax: +49-711 351456-99, e-mail: mail@schweizerbart.de
Internet: http://www.schweizerbart.de
⊘ Gedruckt auf alterungsbeständigem Papier nach ISO 9706-1994

ISSN 1432-8364
Science Citation Index Expanded (also known as SciSearch®) Journal Citation Reports/Science Edition

Erscheinungsweise: 6 Hefte pro Jahrgang.
Bezugspreis im Abonnement: € 239,– pro Jahrgang. Mitglieder der DGPF erhalten die Zeitschrift kostenlos. Der Online-Zugang ist im regulären Subskriptionspreis enthalten.
Anzeigenverwaltung: E. Schweizerbart'sche Verlagsbuchhandlung (Nägele u. Obermiller), Johannesstraße 3A, 70176 Stuttgart, Germany, Tel.: +49-711 351456-0; Fax: +49-711 351456-99.
e-mail: mail@schweizerbart.de, Internet: http://www.schweizerbart.de
Bernhard Harzer Verlag GmbH, Westmarkstraße 59/59a, 76227 Karlsruhe, Germany, Tel.: +49-721 944020, Fax: +49-721 9440230, e-mail: Info@harzer.de, Internet: www.harzer.de
Printed in Germany by Tutte Druckerei & Verlagsservice GmbH, 94121 Salzweg, Germany.

PFG – Jahrgang 2014, Heft 3
Inhaltsverzeichnis

Originalbeiträge

Beiträge aus Wissenschaft und Praxis

Mitteilungen

Zusammenfassungen der „Originalbeiträge“ und der „Beiträge aus Wissenschaft und Praxis“ (deutsch und englisch) sind auch verfügbar unter www.dgpf.de/neu/pfg/ausgaben.htm

PFG 2014 / 3, 0161 – 0173
Stuttgart, June 2014

Article

Geometry and Colour Based Classification of Urban Point Cloud Scenes Using a Supervised Self-Organizing Map

Eric Kenneth Matti & Stephan Nebiker, Muttenz, Schweiz

Keywords: terrestrial laser scanning, fast point feature histogram, self-organizing maps, HSV colour space

Summary: This paper presents a robust approach for directly labelling textured 3D points within complex urban scenes. The approach is primarily based on the specific exploitation of various colour and geometry based point features, namely by calculating the HSV colour values, a fast point feature histogram (FPFH), and the zenith angle to the surface normal per point. The geometrical point features are thereby calculated over two different levels of neighbourhood regions in order to accommodate point density variation. This results in a 71-dimensional feature vector per point, which is used as input for a supervised point classification using a previously trained self-organizing map (SOM). Investigations of the proposed method show, that a 3D point cloud of a real complex urban laser scanning scene can be classified with good to very good accuracy for the object classes "road", "building façade" and "vegetation" but with an inferior performance for the class "tree trunk / branch".

Zusammenfassung: *Geometrie- und farbbasierte Punktwolkenklassifizierung von urbanen Laserscanningszenen mittels überwachter SOM-Klassifikation.* In diesem Beitrag wird eine robuste Methode zur direkten Klassifizierung texturierter 3D-Punkte innerhalb komplexer urbaner Laserscanningszenen vorgestellt. Die Methode basiert auf farblichen und geometrischen Charakteristiken der Punkte. So wird für jeden Punkt sein jeweiliger HSV-Farbwert, sein Fast Point Feature Histogramm und sein Zenitwinkel zur Flächennormalen berechnet. Um dabei variable Punktdichten zu berücksichtigen, werden die geometrischen Punktcharakteristika für zwei unterschiedlich große Nachbarschaftsregionen berechnet. Daraus resultiert ein 71-dimensionaler Featurevektor pro Punkt als Input für die überwachte Punktklassifikation mittels einer trainierten Self-Organizing Map (SOM). Untersuchungen des vorgeschlagenen Verfahrens an einer realen komplexen urbanen Laserscanningszene zeigen auf, dass die Methode in der Lage ist, Punkte nach den Objektklassen Straße, Vegetation und Gebäudefassade mit einer guten bis sehr guten Klassifikationsgenauigkeit zu klassifizieren, jedoch eine geringere Qualität bei der Baumstamm/-ast-Klassifikation erreicht wird.

1 Introduction

The urban space can nowadays be effectively represented by means of dense textured 3D point clouds derived from the recordings of mobile or non-mobile terrestrial laser scanning and image based systems. Apart from the use of such rich point clouds for interactive 3D visualization and measuring purposes (Nebiker et al. 2010), point clouds are widely used as a basis to manually, semi-automatically or at best automatically derive explicit 3D models composed of points, lines, surfaces and volumes.

With recent progress in large scale terrestrial surveying, e.g. by means of mobile or portable TLS (Terrestrial Laser Scanning) systems (Vennegeerts 2010), the automatic derivation of non-geometrical and geometrical object information has become increasingly important in order to efficiently exploit the recorded scenes, such as in order to create various

www.schweizerbart.de
DOI: 10.1127/1432-8364/2014/0216
1432-8364/14/0216 $ 3.50

products, such as 3D city models, or to further understand a recorded scene. Although dense textured 3D point clouds have high geometric and radiometric information content, the automatic robust derivation of further semantic or geometric information and models is not easily achieved. Furthermore, the complex structure of different objects, their arrangement within the world as well as point cloud properties, e.g. outliers in measurements, variations in point density and occlusions, have resulted in the development of various specialized object detection and labelling methods. Thus, among others, algorithms have been developed for extracting geometric primitives (Schnabel et al. 2007, Hohmann et al. 2009, Wan & Sharf 2012), for directly classifying single points (Lim & Suter 2007, Munoz et al. 2009, Rusu et al. 2009, Brodu & Lague 2012, Shapovalov et al. 2010, Xiong et al. 2011, Niemeyer et al. 2012), for detecting objects (Patterson et al. 2008, Golovinskiy et al. 2009, Steder et al. 2009, Teichman et al. 2011, Monnier et al. 2012, Velizhev et al. 2012) and for segmenting point clouds, e.g. by the means of region-growing algorithms (Zhan et al. 2009), graph-based algorithms (Lai et al. 2009, Schoenberg et al. 2010, Strom et al. 2010) or clustering algorithms (Jiang 2004, Liu et al. 2007, Biosca & Lerma 2008, Zhuang et al. 2008).

In this paper, a method for directly labelling 3D points is presented, which exploits a combination of geometric and radiometric properties. It enables the classification of textured points within a complex urban laser scanning scene according to a finite number of disjoint object classes. The method is primarily based on the specific calculation of various colour and geometry based point features, namely the calculation of the HSV colour values, a fast point feature histogram (FPFH) and the zenith angle of the surface normal per point. Similar to Brodu & Lague (2012) the geometrical point features are calculated over two different levels of neighbourhood regions in order to consider point density variations. In doing so, the FPFH values allow to determine if a point is part of a surface, sphere, cylinder, edge or corner, whereas the zenith angle of the surface normal is calculated in order to receive an absolute inclination measure of the underlying surface. In addition to deriving these geometrical point features, the RGB colour values per point are transformed into the HSV colour space in order to receive decorrelated and thus robust colour values. The resulting feature vector is used as input for a point-based classification, using a previously trained self-organizing map (SOM).

In the following section, related work regarding the direct classification of points, also known as point labelling, is presented. After presenting our method and the used algorithms in section 3, investigation results, namely the analysis of the expressiveness of the used point features and the obtainable classification accuracy, are presented in section 4. In the last section, conclusions and an outlook on possible future optimization of the proposed method are given.

2 Related Work

Object detection within point clouds can be viewed as the process of assigning different distinct point subsets to an object class of the real world. In order to distinguish these object classes, a set of geometrical or non-geometrical features characterizing the properties of points belonging to these classes can be analysed. Thus, by calculating features for each point and using a classification method which labels a point according to its features one can implicitly create the point subsets belonging to different object classes. According to Biosca & Lerma (2008), the local point features used should represent the surrounding area as well as possible. In addition, the choice of features also greatly depends on the objects to be distinguished from one another.

In particular, Liu et al. (2007) and Zhuang et al. (2008) both utilize the 3D position, surface normal, mean and Gaussian local curvature for their different segmentation methods, namely a fuzzy-clustering- and SOM-based segmentation. In presence of a textured point cloud, Zhan et al. (2009) and Sareen et al. (2010) both present a region-growing segmentation method solely based on the colour values of each point, whereas Schoenberg et al. (2010) and Strom et al. (2010) use the colour values in addition to the surface normal per point in order to achieve a more robust result

of their graph-based segmentation. In addition to these rather simple point features, there has been considerable work done on making local shape 3D features more discriminative and robust. Amongst others, Patterson et al. (2008) use spin images (Johnson & Hebert 1999) and extended Gaussian images (Horn 1984) for detecting cars, Rusu et al. (2009) use fast point feature histograms (FPFH) in order to assign points to different surfaces, edges or corners, Brodu & Lague (2012) present a multi-scale eigenvalue-based feature in order to characterize the 1D/2D/3D properties of the local scene at each point and at different scales while Flitton et al. (2012) present a novel 3D extension to the visual cortex model, previously used in 2D object recognition (Serre et al. 2005, Mutch & Lowe 2008), for recognizing various objects in 3D volumetric imagery. Furthermore, inspired by the SIFT (Lowe 2004) image feature, Skelly & Sclaroff (2007) present the rotation invariant feature transform (RIFT) and Tombari et al. (2010) the Signature of Histograms of OrienTations (SHOT) feature, both showing promising results for the problem of identifying corresponding points. Finally, we refer to Tombari et al. (2010) and Alexandre (2012) for a comparative evaluation and presentation of further 3D point features.

Besides the point feature choice, various classification methods are proposed for directly classifying single points. On the one hand, point independent classification schemes using a linear discriminant analysis (Brodu & Lague 2012), a support vector machines (Golovinskiy et al. 2009, Rusu et al. 2009, Brodu & Lague 2012) or a random forest (Golovinskiy et al. 2009, Shapovalov et al. 2010) classifier are proposed. On the other hand, classification schemes that consider point context, such as conditional random fields (Lim & Suter 2007, Niemeyer et al. 2012, Rusu et al. 2009), high-order associative Markov network (Munoz et al. 2009) as well as non-associative Markov network (Shapovalov et al. 2010) classifiers or stacked 3-D parsing using a simple K-class logistic regression classifier (Xiong et al. 2011) are proposed, in order to generally achieve a higher classification performance than non-point-context considering approaches.

3 Method

3.1 *Overview*

Our system takes an unclassified textured point cloud as input. As a result, it creates a classified point cloud, in which each point is labelled according to the object class it is most likely to belong to. The system proceeds in three steps, as outlined in Fig. 1. First, we manually extract a set of points for each object class to be detected from the given input point cloud, thus yielding a set of training data. Then the local point features are calculated for both, the training and the test data, namely the HSV colour values $\{h_q, s_q, v_q\}$, the surface normals $\{n_q^{(1)}, n_q^{(2)}\}$, the zenith angles of the surface normal $\{z_q^{(1)}, z_q^{(2)}\}$ and the 33 features of the fast point feature histogram $\{fpfh_{33_q}^{(1)}, fpfh_{33_q}^{(2)}\}$ for each point p_q and the two neighbourhood regions (1) and (2). Finally, the SOM classifier is trained and used to classify each point of the point cloud using the feature vector $[h_q\ s_q\ v_q\ z_q^{(1)}\ z_q^{(2)}\ fpfh_{33_q}^{(1)}\ fpfh_{33_q}^{(2)}]$ having a dimension of 71. The different steps and the prototype implementation are described in detail in the following sections.

3.2 *Transformation of the RGB Colour Values to HSV Colour Values*

Based on the works of Zhan et al. (2009) and Sareen et al. (2010), which both present a re-

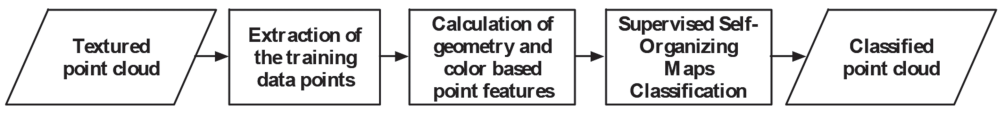

Fig. 1: Schematic representation of the proposed point classifications steps.

gion-growing segmentation method solely using colour values in order to achieve better results compared to geometry-based methods for point clouds with a high degree of outliers and areas of occlusion, as well as on the work of Strom et al. (2010), who also propose to use colour values in addition to surface normals in order to ensure a more robust segmentation performance, we use point colour values to include a non-geometrical local point feature during classification. Due to the high correlation between the colour values in the RGB colour space, the recorded RGB values per point are transformed into the HSV colour space. In this model a colour is primarily characterized by the hue (H) parameter, whereas the saturation (S) and value (V) represent variations of the same hue (H). Thus, resulting in a colour characterization primarily based on a single parameter.

3.3 *Calculation of the Surface Normals and their Zenith Angles*

In order to calculate the zenith angles of the surface normals and the Fast Point Feature Histograms, the surface normal of each point is calculated. The surface normal n_q of a point p_q is calculated according to the principal component analysis (PCA) method originally proposed by Berkmann & Caelli (1994), by calculating the covariance matrix C_q according to (1) using the k-nearest neighbours and by determining its eigenvector $n_0 = n_q$ corresponding to the smallest eigenvalue λ_0.

$$c_q = \frac{1}{k}\sum_{j=1}^{k}\left(p_j - \overline{p}\right)\left(p_j - \overline{p}\right)^T \tag{1}$$

However, since there is no mathematical way to solve for the sign of n_0, the inward or outward orientation of the normals with respect to the underlying surface is unknown. Thus, in order to solve this problem, we orient all normals n_q consistently towards the sensor viewpoint v, as proposed by Rusu (2009), by determining the sign of n_q so that the (2) is satisfied.

$$n_q \cdot (v - p_q) > 0 \tag{2}$$

In order to obtain an absolute geometrical local point feature, enabling inference of the absolute inclination of the underlying surface, the zenith angle z_q of the surface normal n_q is calculated according to (3).

$$z_q = acos\left(\frac{n_q \cdot \left[0\ 0\ 1\right]^T}{\left|n_q\right|}\right) \tag{3}$$

3.4 *Calculation of the Fast Point Feature Histograms (FPFH)*

As a relative geometrical local point feature the fast point feature histogram, as presented in Rusu et al. (2009) and Rusu (2009), is used. The purpose of this feature is to encode local geometrical properties by generalizing the mean curvature around a query point p_q using a multi-dimensional histogram. The feature is invariant to the pose of the underlying surface and copes very well with different sampling densities or noise (Rusu 2009). In addition to this robustness the FPFH has good discriminating properties. According to the comparative study of Alexandre (2012) the FPFH performs well compared to other state of the art 3D features in object and category recognition and has shown to yield excellent results in classifying points (Rusu et al. 2009). The calculation of the FPFH for a point p_q based on its neighbouring points p_k is presented in detail in Alg. 1 and Fig. 2.

1. Calculation of the simplified point feature histogram (SPFH) for point p_q:
   a) Definition of the points p_k constituting the neighbourhood p_q, either by taking all points within a certain range or by taking the n-nearest neighbours (Fig. 2a).
   b) Calculation of the k angles (α, ϕ, θ) between point p_q and p_k:
   By defining a Darboux uvw coordinate frame in one of the points p_q or p_k (Fig. 2b)
   according to, $u = n_s$, $v = u \times \frac{(p_t - p_s)}{\left\|p_t - p_s\right\|_2}$,
   $w = u \times v$ with
   if $\arccos(n_q\, p_{kq}) \leq \arccos(n_k\, p_{qk})$, $p_{kq} = p_q - p_k$, then $p_s = p_q$, $n_s = n_q$ and $p_t = p_k$, $n_t = n_k$ else $p_s = p_k$, $n_s = n_k$ and $p_t = p_q$, $n_t = n_q$

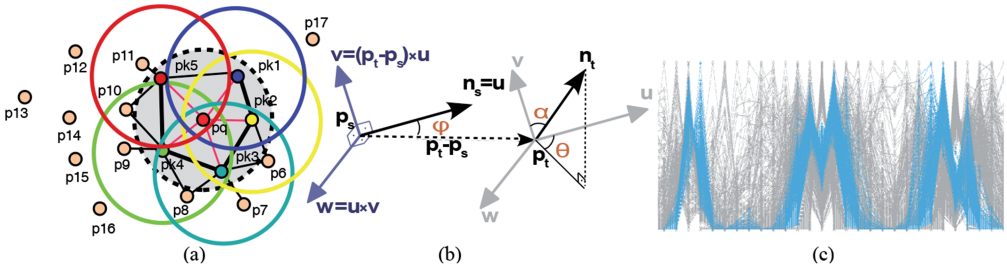

Fig. 2: Illustration of the calculation of the FPFH for point pq adapted from Rusu 2009) in (a) and (b) as well as a parallel coordinate plot of the FPFH's for multiple tree trunk / branch points (highlighted in blue) in (c).

and calculating the angles (α, ϕ, θ) according to $\alpha = v \cdot n_t, \phi = u \cdot \frac{(p_t - p_s)}{\|p_t - p_s\|_2}$,

$$\theta = \arctan(w \cdot n_t, u \cdot n_t)$$

c) Creation of the histogram for the k angles (α, ϕ, θ).

2. Calculation of the simplified SPFH for all neighbouring points p_k as in step 1.
3. Calculation of the FPFH for point p_q according to:

$$FPFH(p_q) = SPFH(p_q) + \frac{1}{k} \sum_{i=1}^{k} \frac{1}{w_k} \cdot SPFH(p_k)$$

with w_k = Distance beween point p_q and p_k.

Alg. 1: Calculation of the FPFH for point pq (according to Rusu 2009).

3.5 *Supervised Self-Organizing Map Classification*

In order to implement a precise as well as fast 3D point classification method a self-organizing map (SOM) was used. In contrast to supervised methods, a SOM, in principle being an unsupervised clustering method, demands significantly less computational resources and scales better to large learning problems (Haykin 1999). Yet, as shown by Vasigh & Kompany-Zareh (2013), it can achieve a similar classification performance as a more powerful support vector machines classification. SOM can also be used for online learning, i.e. the model can be adapted incrementally as new training samples are made available. The choice of using a self-organizing map was additionally motivated by works of Jiang (2004) and Liu et al. (2007), which both achieved good results in segmenting point clouds using a SOM, even for noisy data.

The self-organizing map, a competitive self-learning neural network, developed by Kohonen since 1981, is mainly used to project data of an n-dimensional feature space onto a two-dimensional regular grid of nodes / neurons. By doing so, the original information is compressed, while the most relevant topological and metrical relationships of primary data patterns are preserved. Thus, entities that lie near to one another within the n-dimensional feature space will also come to lie close to one another in the SOM (Kohonen 2001). On the one hand, a SOM can be used for clustering datasets, whereas on the other hand, by applying a slight modification to the algorithm, it can also be used for the classification of datasets. The so-called supervised SOM classification, in principle still an unsupervised learning method, in addition to the n-dimensional feature vectors takes into account their class labels during training. This allows the resulting trained neuron weights to be assigned to a class and, consequently, a test sample to be classified (see following Alg. 2).

Input data:

- Set of training vectors $x_{train}^{(i)} = \left[x^{(i)}, y^{(i)}\right]$

  with vector $x^{(i)} \in \mathbb{R}^n$ containing the N point feature values and $y^{(i)} \in \mathbb{R}^k$ corresponding to the unit label vector with its k^{th} component

set to one if $x^{(i)}$ belongs to the object class k and the rest of its components set to zero.
- Set of vectors $x_{test}^{(ii)} \in \mathbb{R}^n$.

1. Random or linear initialization of the weight vector $m^{(j)} \in \mathbb{R}^{n+k}$ asscociated with each neuron j.
2. Training phase of the SOM:
   For each training step t from 1 to max_iterations:
   a) Random selection of a training vector $x_{train}(t)$ from the set of training vectors.
   b) Comparison of $x_{train}(t)$ with all neuron weight $m^{(j)}$, in order to determine the best matching neuron c according to the chosen similarity measure (i.e., the Euclidean distance).
   c) Modification of the weight vector $m^{(c)}$ of the best matching neuron c and the weight vectors $m^{(j)}$ of the neurons j within a circular neighbourhood of radius $\sigma(t)$ of the best matching neuron c according to:
   $m^{(j)}(t+1) = m^{(j)}(t) + h_{cj}(t)[x_{train}(t) - m^{(j)}(t)]$
   with $h_{cj} = \alpha(t) \cdot e^{-d_{cj}^2/2\sigma^2(t)}$: Gaussian neighbourhood function, $\alpha(t) \in [0, 1]$: learning rate, $d_{cj} \in \mathbb{Z}$: grid distance between neuron c and respective neuron j and $\alpha(t) \in [0, \text{max\_som\_size}]$: neighbourhood distance. $\alpha(t)$ and $\sigma(t)$ are monotonically decreasing functions over time t in our case linear functions with negative slope (section 4).
3. Classification phase using the trained SOM:
   Each test vector $x_{test}^{(ii)}$ is compared to the x-part (the first N components corresponding to the features) of all trained neuron weights $m^{(j)}$, in order to determine the best matching neuron c according to the chosen similarity measure. The point's class membership is then given by the index of the largest component of the y-part (the last K components corresponding to the label vector) of $m^{(c)}$.

Alg. 2: Supervised SOM classification (according to Kohonen 2001).

3.6 *Prototype Implementation*

A first prototype of the proposed labelling method was implemented by using Python as a wrapper for calculating the point features using the point cloud library (Rusu & Cousins 2011) and for performing the supervised SOM classification using Matlab's SOM toolbox (Alhoniemi et al. 2012).

4 Investigations

4.1 *Test, Training and Reference Datasets*

For the investigation of the expressiveness of the point features and of the overall classification accuracy, a point cloud of an urban region, recorded from two locations with a Leica ScanStation 2, was used. The recorded scene has the dimension of 100 m × 70 m × 15 m, contains over 1 million points and is shown in Fig. 3a. Apart from a high inter and intra object class variance within the scene, e.g. for vegetation, the point cloud contains variations in point density, occluded areas and, due to using the on-board capabilities of the Leica ScanStation 2, is generally poorly textured (see Fig. 3a).

Based upon this unclassified point cloud the training and the reference datasets were created. The training dataset was created by manually extracting small regions corresponding to the object classes "building façade", "road", "vegetation", and "tree trunk / branch". In this process regions of different point densities per object class were selected in order to account for any inter-class variation of the derived point features. The final training dataset consists of 100,000 points. The point count per object class is equal to 10% of the number of points of that class in the reference (see Tab. 2). The reference data was created by manually labelling the rest of the entire unclassified point cloud according to the object classes to be detected.

4.2 *Expressiveness of the used Point Features*

During the feature design phase various graphical exploratory data analysis methods were used, in order to primarily determine whether the selected point features allow

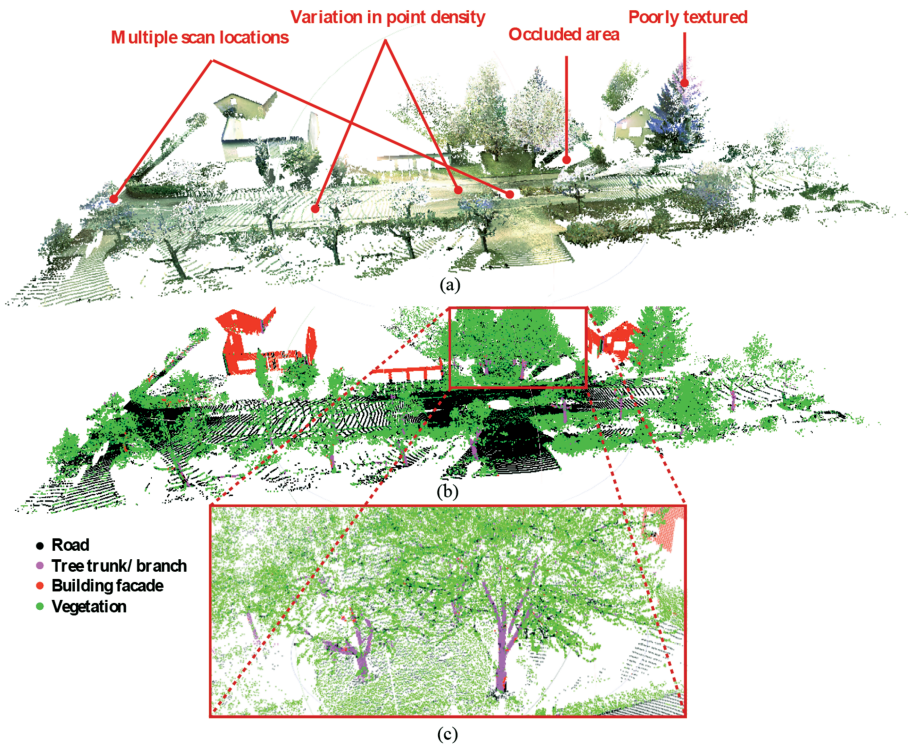

Fig. 3: Original textured point cloud (a) with examples of typical problems such as variations in point density, occluded areas and poor texturing. Classified point cloud (b) and a detail (c).

for a distinction between the selected object classes to be detected and which of the features are the most expressive ones. First, a matrix of pairwise scatter plots of the four point features h_q, s_q, v_q and z_q of training data subsets with similar point density was generated. Fig. 4 illustrates that the HSV colour values allow a partial separation of the object classes "building façade" and "road" from the classes "tree trunk / branch" and "vegetation", but the zenith angle of the surface normal needs to be taken into account in order to separate the object classes "tree trunk / branch" and "vegetation", overlapping in the HSV colour space. Furthermore, it can be seen, that the zenith angles of the vegetation class have a high variance and that therefore some points nevertheless come to lie within the region mainly occupied by points belonging to the object class "tree trunk / branch". The reason for this high zenith angle variance is that the vegetation training sample contains both points of the ground vegetation and leaves on the trees, with the latter vegetation subclass having an especially high zenith angle variance.

For further investigation of the expressiveness of the calculated point features, the values of the 37-dimensional feature vector $[h_q\, s_q\, v_q\, z_q\, fpfh_{33_q}]$ for a training data subset with similar point density were visualized using an interactive and dynamic grand tour visualization (Asimov 1985, Buja & Asimov 1986). This multi-dimensional visualization technique generally maps the values of an n-dimensional feature space using a linear combination to a lower dimensional feature space. Thus, it is a useful technique for visually analysing the distribution of and for identifying clusters within multivariate data. In order to perform an optimal visual cluster analysis, we projected the values of the 37-dimensional feature vectors into the orthogonal coordinate frame defined by their principal components and determined the projection parameters us-

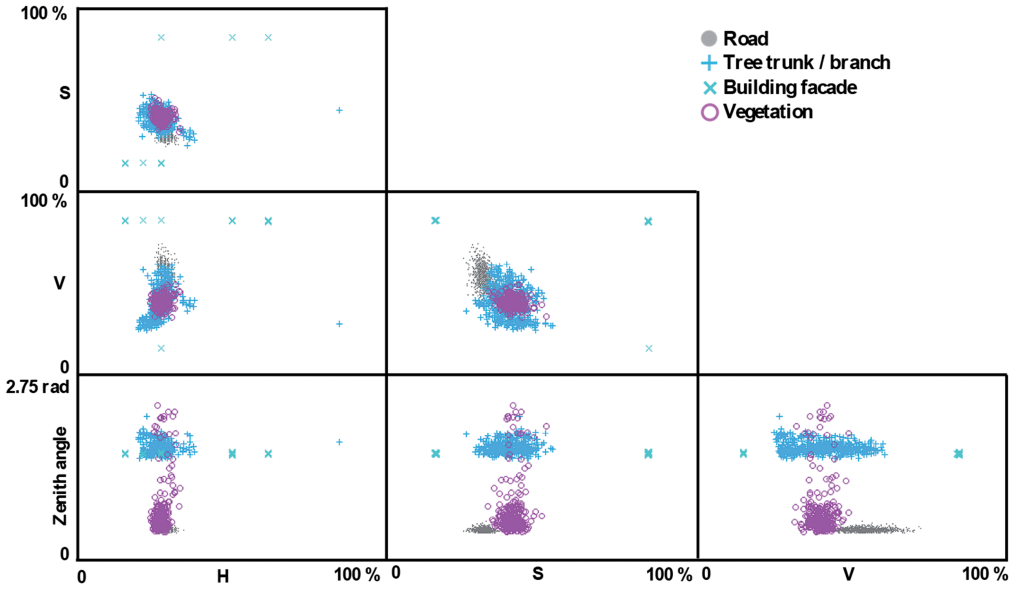

Fig. 4: Scatterplot matrix of the HSV colour values and the zenith angle of the surface normals (using 32 nearest neighbours for the surface normal calculation).

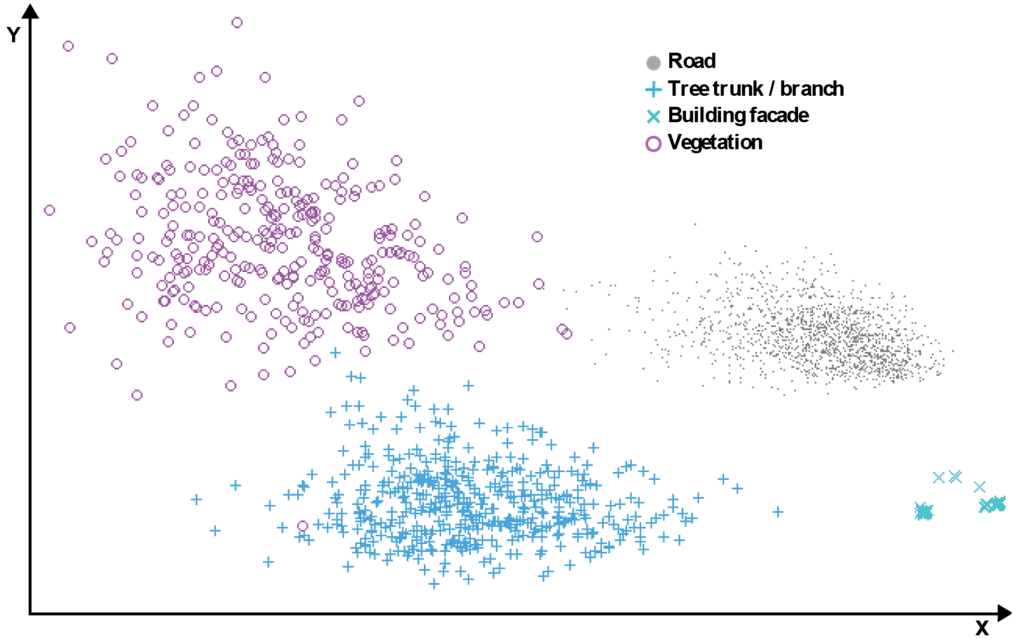

Fig. 5: Grand Tour Visualization of the HSV colour, the zenith angle of the surface normals and the FPFH values per point (using 32 nearest neighbours for the surface normal and FPFH calculation).

ing a Linear Discriminant Analysis (LDA) (Cook et al. 1995, Cook & Swayne 2007). Fig. 5 shows that by using the HSV colour, zenith angle and FPFH values, all the points belonging to each object class form a distinct cluster, which is different to the case in Fig. 4, when FPFH were not used. This provides a visual indication that the selected point features are expressive enough to classify the points according to the examined object classes and under the assumption of similar point density.

4.3 *Classification Accuracy*

In order to numerically quantify the achievable classification accuracy for various parameterizations of the proposed point labelling method, a manually labelled reference dataset was created (see section 4.1 for further details). This enables the calculation of confusion matrices and various quality measures by comparing each point's object class membership resulting from the classification with its actual membership. All of the following classification results are based upon using the supervised SOM classification functionality of Matlab's SOM toolbox (Alhoniemi et al. 2012). The linear initialized, 100 x 100 sized SOM of hexagonal lattices was thereby trained according to Alg. 2 using a two-phased training scheme and the parameters presented in Tab. 1.

Tab. 2 shows the resulting classification accuracy of a single-scale approach using the HSV, the zenith angle and FPFH values per point as input for the supervised SOM classification. The geometrical features were calculated using the 32 nearest neighbouring points. Tab. 2 shows that the precision for all classes, except for the class "tree trunk / branch", lies

Tab. 1: Parameterization of the rough (a) and fine-tuning (b) phase of the SOM training.

Parameter	Value
Max. iterations	15 x number of neurons$^{(a)}$, 60 x number of neurons$^{(b)}$
$\alpha(t)$ (Learning rate)	Linear decreasing function from 0.5 to 0.05$^{(a)}$ and 0.05 to 0.0$^{(b)}$
$\sigma(t)$ (Neighbourhood radius)	Linear decreasing function from $m/8$ to $m/32^{(a)}$ and $m/32$ to $1^{(b)}$, with m = maximal SOM side length / SOM size

Tab. 2: Confusion matrix and classification accuracy using both colour and geometrical features composed of the HSV values as well as the single set of zenith angles and FPFH values calculated using 32 nearest neighbours.

		Reference data					
		Road	Tree trunk / branch	Building façade	Vegetation	Total amount of points	Precision (%)
Classification	Road	597,217	4,578	15,040	127,935	744,770	80
	Tree trunk / branch	1,903	6,937	238	1,183	10,261	68
	Building façade	25	14	23,131	87	23,257	99
	Vegetation	25,151	12,075	1,264	298,864	337,354	89
Total amount of points		624,296	23,604	39,673	428,069	1,115,642	
Recall (%)		96	29	58	70		
Overall classification accuracy (%)		83					

above 80%. In contrast, the recall for all classes is generally unsatisfying, with only the points of the class "road" having a recall rate of 96%. The analysis of this poor classification result shows that the majority of the misclassifications occur in areas where the point density is sparse and hence the consideration of only 32 neighbouring points while calculating the geometrical features is not sufficient.

Tab. 3, in contrast, shows the classification accuracy achieved in two experiments involving geometrical features obtained from two neighbourhoods. The results shown in bold font were achieved using the HSV values, the two sets of zenith angle values using 8 and 128 nearest neighbouring points and the two sets of FPFH values using 8 and 32 neighbouring points. The results shown in regular font were obtained by using the same point features, but neglecting the HSV values. The results show that the precision and recall rate for all classes, except for the class "tree trunk / branch", now are above 91% and 87%, respectively. Furthermore, the results show that the additional consideration of colour values results in a more accurate classification, especially for the geometrically similar road and ground vegetation points. Analysing the relatively poor classification result for the object class "tree trunk / branch" it was found that the majority of misclassifications are due to the challenging problem of correctly distinguishing between leaves and branches for each point while creating the reference dataset (see Fig. 3c). Hence, the classification results for this object class can be considered as too pessimistic. Comparing our best classification results presented in Tab. 3 to other terrestrial point cloud labeling methods with comparable object classes, we achieve a nine percent lower and two percent higher overall classification accuracy than Lim & Suter (2007) and Munoz et al. (2009), respectively. As these results were achieved on different datasets, this comparison is not conclusive. Nevertheless, it shows that a similar classification performance is achieved.

In summary, the proposed point labelling method, using both colour and multi-scale geometrical point features, allows for a moderately accurate classification of points belonging to object class "tree trunk / branch", while achieving good to very good classification results for the object classes "road", "building façade" and "vegetation". Additionally,

Tab. 3: Confusion matrix and classification accuracy using both colour and geometrical features composed of the HSV values, the two sets of zenith angles using 8 and 128 nearest neighbours and the two sets of FPFH values using 8 and 32 nearest neighbours (bold font). In comparison, the values in regular font show the results obtained without the colour features.

		Reference data					
		Road	Tree trunk / branch	Building façade	Vegetation	Total amount of points	Precision (%)
Classification	Road	600,257 558,519	4,200 3,993	1,520 1,402	52,203 70,192	658,180 634,106	91 88
	Tree trunk / branch	413 488	10,086 9,885	127 761	4,094 3,225	14,720 14,359	69 69
	Building façade	331 603	1,206 909	36,876 36,719	1,347 1,462	39,760 39,693	93 93
	Vegetation	23,295 64,686	8,112 8,817	1,150 791	370,425 353,190	402,982 427,484	92 83
Total amount of points		624,296	23,604	39,673	428,069	1,115,642	
Recall (%)		96 89	43 42	93 93	87 83		
Overall classification accuracy (%)		91 86					

the presented classification results show two properties of the used features that result in a better overall classification. Firstly, the HSV colour values support a correct classification of geometrically similar object classes and secondly, by calculating the geometrical point features over two levels of neighbourhood regions, point density variations are accounted for.

5 Conclusion

This paper presents an approach for classifying textured points within a complex urban point cloud according to a distinct set of object classes. By using the HSV colour values as well as the zenith angle and the Fast Point Feature Histogram (FPFH) values, calculated over two different local neighbourhoods, as point features as an input to a supervised SOM classification, we were able to classify points according to the object classes "road", "tree trunk / branch", "building façade" and "vegetation". Our investigations show that the selected 3D point features are sufficiently expressive for labelling points according to the examined object classes under the assumption of constant point density. Secondly, by using a supervised SOM classifier, the features allow the classification of a poorly textured point cloud affected by occlusion and density variations with a good overall classification accuracy of 91%, but with a relatively poor recall for the challenging object class "tree trunk / branch". Our work further supports the known fact that the features used for classification have a large influence on achieving optimal results and thus must be designed according to the object classes to be distinguished from one another. In our application we thus selected point features allowing the separation of various objects of different colours, absolute surface inclinations, and shapes within a point cloud of varying point density. Future work will focus on the further development of the proposed method, on combining different features to a multi-scale / multi-modal point feature in dependency of the classification task, by including an approach for automatically determining the size and amount of required neighbourhood regions, e.g. Demantké et al. 2011, as well as the features needed for optimal classification.

References

Alexandre, A., 2012: 3D Descriptors for Object and Category Recognition : A Comparative Evaluation. – IEEE/RSJ International Conference on Intelligent Robots and Systems (IROS), Vilamoura, Portugal.

Alhoniemi, E., Himberg, J., Parhankangas, J. & Vesanto, J., 2012: SOM Toolbox. – http://www.cis.hut.fi/somtoolbox/ (24.4.2012).

Asimov, D., 1985: The Grand Tour: A Tool for Viewing Multidimensional Data. – SIAM Journal on Scientific Computing **6** (1): 128–143.

Berkmann, J. & Caelli, T., 1994: Computation of Surface Geometry and Segmentation using Covariance Techniques. – IEEE Transactions on Pattern Analysis and Machine Intelligence **16** (11): 1114–1116.

Biosca, J.M. & Lerma, J.L., 2008: Unsupervised Robust Planar Segmentation of Terrestrial Laser Scanner Point Clouds Based on Fuzzy Clustering Methods. – ISPRS Journal of Photogrammetry and Remote Sensing **63** (1): 84–98.

Brodu, N. & Lague, D., 2012: 3D Terrestrial Lidar Data Classification of Complex Natural Scenes using a Multi-Scale Dimensionality Criterion: Applications in geomorphology. – ISPRS Journal of Photogrammetry and Remote Sensing **68** (0): 121–134.

Buja, A. & Asimov, D., 1986: Grand Tour Methods: An Outline. – Computing Science and Statistics **17:** 63–67.

Cook, D., Buja, A., Cabrera, J. & Hurley, C., 1995: Grand Tour and Projection Pursuit. – Journal of Computational and Graphical Statistics **4** (3): 155–172.

Cook, D. & Swayne, D.F., 2007: Interactive and Dynamic Graphics for Data Analysis. – With R and GGobi, Springer.

Demantké, J., Mallet, C., David, N. & Vallet, B., 2011: Dimensionality Based Scale Selection in 3D LIDAR Point Clouds. – ISPRS Workshop Laser Scanning: 97–102, Calgary, Alberta, Canada.

Flitton, G., Breckon, T.P. & Megherbi, N., 2012: A 3D Extension to Cortex Like Mechanisms for 3D Object Class Recognition. – IEEE Conference on Computer Vision and Pattern Recognition (CVPR): 3634–3641, Los Alamitos, CA, USA.

Golovinskiy, A., Kim, V.G. & Funkhouser, T., 2009: Shape-Based Recognition of 3D Point Clouds in Urban Environments. – International

Conference on Computer Vision (ICCV): 2154–2161, Kyoto, Japan.

Haykin, S., 1999: Neural Network. – Second Edition, MacMillan College Publishing Company, London, UK.

Hohmann, B., Krispel, U., Havemann, S. & Fellner, D., 2009: Cityfit: High-Quality Urban Reconstructions by Fitting Shape Grammars to Images and Derived Textured Point Clouds. – 3D Virtual Reconstruction and Visualization of Complex Architectures, Trento, Italy.

Horn, B.K.P., 1984: Extended Gaussian images. – IEEE **72** (12): 1671–1686.

Jiang, B., 2004: Extraction of Spatial Objects from Laser-Scanning Data using a Clustering Technique. – XXth ISPRS Congress, Technical Commission **III:** 219–224, Istanbul, Turkey.

Johnson, A. & Hebert, M., 1999: Using Spin Images for Efficient Object Recognition in Cluttered 3D Scenes. – IEEE Transactions on Pattern Analysis and Machine Intelligence **21** (5): 433–449.

Kohonen, T., 2001: Self-Organizing Maps. – Third Edition, Springer, Heidelberg, Germany.

Lai, Y.-K., Hu, S.-M., Martin, R.R. & Rosin, P.L., 2009: Rapid and Effective Segmentation of 3D Models using Random Walks. – Computer Aided Geometric Design **26** (6): 665–679.

Lim, E.H. & Suter, D., 2007: Conditional Random Field for 3D Point Clouds with Adaptive Data Reduction. – International Conference on Cyberworlds: 404–408, Hannover, Germany.

Liu, X.-M., Zhong, S.-S. & Bai, X.-L., 2007: A Modified SOFM Segmentation Method in Reverse Engineering. – Eighth ACIS International Conference on Software Engineering, Artificial Intelligence, Networking, and Parallel/Distributed Computing: 570–573, Qingdao, China.

Lowe, D.G., 2004: Distinctive Image Features from Scale-Invariant Keypoints. – International Journal of Computer Vision **60** (2): 91–110.

Monnier, F., Vallet, B. & Soheilian, B., 2012: Trees Detection from Laser Point Clouds Acquired in Dense Urban Areas by a Mobile Mapping System. – XXIInd ISPRS Congress, Technical Commission **III:** 245–250, Melbourne, Australia.

Munoz, D., Vandapel, N. & Hebert, M., 2009: Onboard Contextual Classification of 3-D Point Clouds with Learned High-order Markov Random Fields. – IEEE International Conference on Robotics and Automation: 4273–4280, Piscataway, NJ, USA.

Mutch, J. & Lowe, D., 2008: Object Class Recognition and Localization Using Sparse Features with Limited Receptive Fields. – International Journal of Computer Vision **80** (1): 45–57.

Nebiker, S., Bleisch, S. & Christen, M., 2010: Rich Point Clouds in Virtual Globes – A New Paradigm in City Modeling? Computers, Environment and Urban Systems **34** (6): 508–517.

Niemeyer, J., Rottensteiner, F. & Soergel, U., 2012: Conditional Random Fields for LIDAR Classification in Complex Urban Areas. – XXIInd ISPRS Congress, Technical Commission **III:** 263–268, Melbourne, Australia.

Patterson, A., Mordohai, P. & Daniilidis, K., 2008: Object Detection from Large-Scale 3D Datasets using Bottom-up and Top-down Descriptors. – ECCV 2008: 10th European Conference on Computer Vision: 553–566, Marseille, France.

Rusu, R.B., 2009: Semantic 3D Object Maps for Everyday Manipulation in Human Living Environments. – Ph.D. Computer Science Department, Technische Universität München, Germany.

Rusu, R.B., Holzbach, A., Blodow, N. & Beetz, M., 2009: Fast Geometric Point Labeling using Conditional Random Fields. – IEEE/RSJ International Conference on Intelligent Robots and Systems: 3212–3217, St. Louis, MO, USA.

Rusu, R.B. & Cousins, S., 2011: 3D is here: Point Cloud Library (PCL). – IEEE International Conference on Robotics and Automation (ICRA): 1–4, Shanghai, China.

Sareen, K., Knopf, G. & Canas, R., 2010: Rapid Clustering of Colorized 3D Point Cloud Data for Reconstructing Building Interiors. – ISOT 2010 International Symposium on Optomechatronic Technologies: 1–6, Toronto, ON, Canada.

Schnabel, R., Wahl, R. & Klein, R., 2007: Efficient RANSAC for Point-Cloud Shape Detection. – Computer Graphics Forum **26** (3): 1–12.

Schoenberg, J., Nathan, A. & Campbell, M., 2010: Segmentation of Dense Range Information in Complex Urban Scenes. – IEEE/RSJ International Conference on Intelligent Robots and Systems: 2033–2038, Taipei, Taiwan.

Serre, T., Wolf, L. & Poggio, T., 2005: Object recognition with features inspired by visual cortex. – IEEE Computer Society Conference on Computer Vision and Pattern Recognition **2:** 994–1000.

Skelly, L.J. & Sclaroff, S., 2007: Improved Feature Descriptors for 3D Surface Matching. – SPIE Conference on Two- and Three-Dimensional Methods for Inspection and Metrology V 6762.

Shapovalov, R., Velizhev, A. & Barinova, O., 2010: Non-Associative Markov Networks for 3D Point Cloud Classification. – ISPRS Technical Commission III Symposium, PCV 2010 – Photogrammetric Computer Vision and Image Analysis: 103–108, Saint-Mandé, France.

Steder, B., Grisetti, G., Van Loock, M. & Burgard, W., 2009: Robust On-line Model-based Object Detection from Range Images. – IEEE/RSJ International Conference on Intelligent Robots and Systems: 4739–4744, St. Louis, MO, USA.

Strom, J., Richardson, A. & Olson, E., 2010: Graph-Based Segmentation for Colored 3D Laser Point Clouds. – IEEE/RSJ International Conference on Intelligent Robots and Systems: 2131–2136, Taipei, Taiwan.

Teichman, A., Levinson, J. & Thrun, S., 2011: Towards 3D Object Recognition via Classification of Arbitrary Object Tracks. – IEEE International Conference on Robotics and Automation (ICRA): 4034–4041, Shanghai, China.

Tombari, F., Salti, S. & Stefano, L., 2010: Unique Signatures of Histograms for Local Surface Description. – 11th European Conference on Computer Vision (ECCV): 356–369, Hersonissos, Greece.

Vasighi, M. & Kompany-Zareh, M., 2013: Classification Ability of Self Organizing Maps in Comparison with Other Classification Methods. – MATCH Communications in Mathematical and in Computer Chemistry **70:** 29–44.

Velizhev, A., Shapovalov, R. & Schindler, K., 2012: Implicit Shape Models for Object Detection in 3D Point Clouds. – XXIInd ISPRS Congress, Technical Commission **III:** 79–184, Melbourne, Australia.

Vennegeerts, H., 2010: Objektraumgestützte kinematische Georeferenzierung für Mobile-Mapping-Systeme. – Ph.D. Fakultät für Bauingenieurwesen und Geodäsie, Leibniz Universität Hannover, Germany.

Wan, G. & Sharf, A., 2012: Grammar-Based 3D Facade Segmentation and Reconstruction. – Computers Graphics **36** (4): 216–223.

Xiong, X., Munoz, D., Bagnell, J.A. & Hebert, M., 2011: 3-D Scene Analysis via Sequenced Predictions over Points and Regions. – IEEE International Conference on Robotics and Automation (ICRA), Shanghai, China.

Zhan, Q., Liang, Y. & Xiao, Y., 2009: Color-Based Segmentation of Point Clouds. – Laserscanning **09:** 248–252, Paris, France.

Zhuang, J., Liu, X. & Hou, X., 2008: The Fuzzy Clustering Algorithm Based on Weighted Distance Measures for Point Cloud Segmentation. – 2008 Second International Symposium on Intelligent Information Technology Application (IITA): 51–54, Shanghai, China.

Address of the Authors:

Eric Kenneth Matti & Prof. Dr. Stephan Nebiker, FHNW University of Applied Sciences and Arts Northwestern Switzerland, Institute of Geomatics Engineering, CH-4132 Muttenz, Tel.: +41-61-467-4242, Fax: +41-61-467-4460, e-mail: {eric.matti} {stephan.nebiker}@fhnw.ch

Manuskript eingereicht: Mai 2013
Angenommen: Februar 2014

PFG 2014 / 3, 0175–0188
Stuttgart, June 2014

Article

The Metrology of Directional, Spectral Reflectance Factor Measurements Based on Area Format Imaging by UAVs

Eija Honkavaara, Lauri Markelin, Teemu Hakala & Jouni Peltoniemi, Masala, Finland

Keywords: reflectance, radiometry, hyperspectral, unmanned airborne vehicle, metrology

Summary: Remote sensing based on unmanned airborne vehicles (UAVs) is a rapidly developing field of technology. New UAV sensing techniques provide attractive possibilities for measuring the reflectance properties of surfaces using vertical and oblique views. Managing the uncertainties of the reflectance measurements is crucial in many UAV remote sensing applications. We have developed a traceable procedure for conducting reflectance measurements using UAVs. It makes use of a spectrometric measurement system that is based on a UAV and a spectral imager that collects area format spectral data cubes with stereoscopic and multi-view setups. The procedure is based on reflectance panels that are positioned in the area of interest. In this investigation, we investigated the traceability of the radiometric image data processing chain. In order to take care of the uncertainty propagation, we estimated the variance-covariance propagation for the radiometric processing chain. We used the new procedure to calculate the reflectance mosaic and conduct the bidirectional reflectance factor (BRF) measurements. The estimated uncertainties were on the level of 0.01–0.04 in reflectance units.

Zusammenfassung: *Messung von gerichteten Reflektanzen bei hyperspektralen Flächenkameras auf UAVs.* Fernerkundung mit UAVs entwickelt sich derzeit schnell. Neue Aufnahmetechnologien bieten interessante Möglichkeiten zur Messung der Reflexionseigenschaften von Oberflächen. Die Beherrschung des Fehlerbudgets der Strahlungsmessungen ist für viele fernerkundliche Anwendungen entscheidend. Für den Fall der UAVs haben wir die Fehlerfortpflanzung modelliert und eine Transformationskette aufgebaut, die die Messergebnisse rückverfolgen lässt. Die Methode nutzt UAV-gestützt Hyperspektralflächenkameras für Senkrecht- und Schrägaufnahmen. Aus drei der 35 verfügbaren Kanäle wurde dann ein Orthophotomosaik der Reflektanzen erstellt und der BRF (bi-directional reflectance factor) berechnet. Als radiometrische Referenz dienten auf dem Boden ausgelegte Referenzpaneele. Zur Modellierung der Fehlerfortpflanzung schätzen wir die Varianz-Kovarianz-Matrix. Die Fehlerschätzung ergab eine Größenordnung von 0.01–0.04 der Reflektanzeinheiten.

1 Introduction

Remote sensing based on unmanned airborne vehicles (UAVs) is a rapidly developing field of technology. UAVs enable accurate, flexible, and low-cost measurements of 3D geometric, radiometric, and temporal properties of land and vegetation using cameras and other instruments. UAV sensor technology is developing rapidly and several different spectrometric imaging techniques are already available, even for light-weight systems (Hruska et al. 2012, Zarco-Tejada et al. 2012, Buettner & Roeser 2014, Saari et al. 2013).

UAVs are increasingly utilized for various environmental remote sensing applications such as for precision agriculture or water quality monitoring. They also offer an attractive alternative for producing reflectance reference measurements for a satellite sensor and image calibration and validation (cal/val) or for investigating the reflection characteristics of different surfaces and objects. For all these applications, the quality of the collected reflectance data is of great importance.

www.schweizerbart.de
DOI: 10.1127/1432-8364/2014/0218
1432-8364/14/0218 $ 3.50

Reflectance measurement by UAVs has been investigated in several recent investigations. Central challenge in the passive imaging is the impact of view and illumination geometry on the measured reflectance. This dependency is modelled by using a bidirectional reflectance distribution function (BRDF) (Schaepman-Strub et al. 2006). Hakala et al. (2010) used a micro UAV equipped with a consumer-level RGB camera to take directional reflectance measurements of snow. The results were promising; the authors concluded that the method should be further developed. Also Grenzdörffer & Niemeyer (2011) used area-format RGB images, but their approach was based a multi-camera system with vertical and oblique viewing cameras. Schwarzbach et al. (2009), Hueni et al. (2013) and Burkart et al. (2014) installed a spectrometer in a UAV to measure directional reflectance. By integrating a field spectrometer and the airborne spectrometer, these systems were able to achieve very accurate directional reflectance measurements. These investigations have proven the feasibility of the UAVs for the reflectance measurement, but also needs for further development have been identified, such as improving the spectral properties of sensors used or improving the level of automation.

SI traceability is the core concept of metrology, which is the science of measurement; it embraces both experimental and theoretical determinations at any level of uncertainty in any field of science and technology. The Bureau International des Poids et Mesures (BIPM 2004) defines metrological traceability as the "property of a measurement result whereby the result can be related to a reference through a documented unbroken chain of calibrations, each contributing to the measurement uncertainty". The level of traceability establishes the level of comparability of the measurement: Whether the result of a measurement can be compared to the previous one, to a measurement result from a year ago, or to the result of a measurement performed anywhere else in the world. Furthermore, the rigorous quantitative analysis methods can only be used for data that have been calibrated to the physical quantities. We think that traceability is an important aspect in many UAV applications.

The objective of our investigation is to develop a SI-traceable procedure for reflectance data generation based on a spectrometric UAV imaging system. In the procedure implemented at the Finnish Geodetic Institute (FGI), the steps in the reflectance transfer process are as follows: Availability of an SI-traceable reflectance standard in a national standards laboratory > Traceable reflectance at the FGI laboratory > Traceable reflectance at the measurement site > Traceable reflectance in the UAV output data. The reflectance standard can be obtained from the Metrology Research Institute at Aalto University, which is the Finnish national standards laboratory for optical quantities. Our focus is on a new kind of a spectral imager collecting area-format images, with spatially overlapping spectral data cubes in the spectral range of 400 nm – 900 nm (Saari et al. 2013, Honkavaara et al. 2013). Furthermore, in this investigation, our specific objective is to study the uncertainty resulting during the last phase of the process, the traceable reflectance in the UAV output data, which has not been rigorously studied in previous studies. This is done by developing uncertainty propagation for the image data post-processing phase.

In the following pages, we first consider the uncertainty propagation of image-based reflectance measurements in section 2. Then, we describe the method developed at the FGI in more detail in section 3. Section 4 describes an empirical campaign and in section 5 we discuss our results. Finally, we provide some conclusions based on our findings in section 6.

2 Uncertainty Propagation of Image-Based Reflectance Measurements

2.1 *Reflectance Measurement Based on Area-Format UAV Images*

The FGI system derives bidirectional reflectance factors (BRFs) using area-format images. BRF is defined as the ratio of the radiation reflected by a target of size dA ($L_s(\theta_i,\varphi_i,\theta_r,\varphi_r)$) to the radiation reflected by an ideal white isotropic (Lambertian) reflector of the same

size with similar illumination conditions ($L_{id}(\theta_i,\varphi_i)$):

$$R_s(\theta_i,\varphi_i,\theta_r,\varphi_r) = L_s(\theta_i,\varphi_i,\theta_r,\varphi_r)/ L_{id}(\theta_i,\varphi_i). \quad (1)$$

θ_i and θ_r are illumination and reflected light (observation) zenith angles, while φ_i and φ_r are the incident and reflected light azimuth angles, as shown in Fig. 1 (Schaepman-Strub et al. 2006, Suomalainen et al. 2009).

For low-altitude imagery, the central radiation components entering the sensor ($L_{at\_sensor}(\lambda)$) include the sunlight ($L_{su}(\lambda)$) and diffuse radiance ($L_{sd}(\lambda)$) reflected by the surface (adopted from Schowengerdt 2007):

$$\begin{aligned} L_{at\_sensor}(\lambda) &= L_{su}(\lambda) + L_{sd}(\lambda) \\ &= \rho(\lambda,\theta_i,\varphi_i,\theta_r,\varphi_r)\, \tau_v(\lambda)\, \tau_s(\lambda)\, E_0(\lambda) \\ &\quad \cos(\theta(x,y))/\pi \\ &\quad + F(x,y)\, \rho(\lambda, 2\pi, \theta_r, \varphi_r)\, \tau_v(\lambda) \\ &\quad E_d(\lambda)/\pi, \end{aligned} \quad (2)$$

where $\rho(\lambda, \theta_i, \varphi_i, \theta_r, \varphi_r)$ is the bidirectional spectral reflectance distribution function (BRDF) and $\rho(\lambda,2\pi,\theta_r,\varphi_r)$ is the reflectance distribution function for diffuse light, while $\tau_v(\lambda)$ and $\tau_s(\lambda)$ are the atmospheric transmittance in the view and solar paths, respectively, $E_0(\lambda)$ is the spectral irradiance on top of the atmosphere, $E_d(\lambda)$ is the spectral irradiance at the surface due to diffuse illumination, and θ is the solar incidence angle on a surface. θ_i and θ_r are the illumination and reflected light zenith angles and φ_i and φ_r are the azimuth angles, respectively. F(x,y) is the fraction of hemisphere visible to the sensor. The UAV system measures the BRF, which is directly linked to BRDF and can thus be solved based on (2).

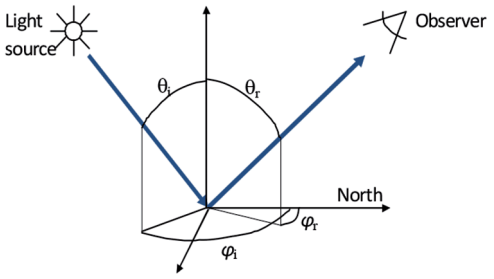

Fig. 1: Bidirectional reflectance geometry. θ_i, φ_i and θ_r, φ_r are zenith and azimuth angles of incident and reflected light, respectively.

The object is observed from different directions in the area-format images. Because of this, the images provide directional reflectance data and the field of view (FOV) of the camera determines the range of the observation angles. Two fundamentally different measurement setups that provide object reflectance are vertical block imaging and oblique BRF block imaging:

- The vertical block is collected with the camera's optical axis pointing down. The FOV of the camera determines the observation angles to the object.
- In the case of the oblique BRF block, the camera's optical axis is tilted from the vertical direction. The UAV is used to collect images around the object to provide a wide range of observation angles. The camera tilt and image FOV determine the possible observation angles.

A characteristic feature in area-format UAV imaging is that a large number of images are needed to cover the desired object area; in other words, thousands of small images are needed to provide an image mosaic for the area of 1 km x 1 km. Dozens of observations from different directions are taken for each object point.

In order to calculate the quantities of the view/illumination geometry, the solar elevation, the 3D model of the object's surface and the orientations of the images are needed. The exact view angles to the object are obtained by using the ground coordinates of the object and the position of the perspective centre. To solve the BRF, information about diffuse light and other atmospheric influences are needed. The image processing chain includes image corrections based on laboratory calibration, a determination of the orientations, digital surface model (DSM) generation, a determination of the atmospheric parameters (and radiometric model parameters), and finally, the reflectance data generation.

2.2 *Uncertainty Propagation*

In this investigation, we are assuming that the geometric quantities can be solved with a suf-

ficient degree of accuracy, and then the major remaining uncertainty components in the BRF measurement include the noise of the CCD or CMOS image, σ_{DN}, and the uncertainty of the reflectance transformation.

The reflectance transformation maps the image's digital numbers (DNs) onto the BRFs ($R(\theta_i,\varphi_i,\theta_r,\varphi_r)$):

$$R(\theta_i,\varphi_i,\theta_r,\varphi_r) = f(x), \quad (3)$$

where f(x) is the function that carries out the reflectance transformation; the *x* includes DNs and other parameters related to the reflectance transformation.

By assuming that x stands for random variables, the uncertainty of an output reflectance (σ_R) can be determined by using variance-covariance propagation techniques (Mikhail 1976):

$$\sigma_R^2 = J_f \Sigma_f J_f^T, \quad (4)$$

where J_f is the Jacobian matrix of f(x) and Σ_f is the variance-covariance matrix of the variables in the model. If we assume a simplified model where there is no correlation between the variables, the estimated standard deviation of the output reflectance value σ_R based on variance-covariance propagation is thus:

$$\sigma_R = \sqrt{\left(\frac{\partial f}{\partial x_1}\right)^2 \sigma_{x_1}^2 + \ldots + \left(\frac{\partial f}{\partial x_n}\right)^2 \sigma_{x_n}^2}. \quad (5)$$

2.2.1 Image noise

The noise in a digital image can either be a constant (fixed pattern noise) or a random type of noise (Sandau 2010). The fixed pattern noise can be eliminated to a large extent based on the laboratory calibration factors, and so achieving an accurate laboratory calibration is an essential part of the data processing chain. Important corrections include corrections for detector array nonuniformities (so-called photo response nonuniformity (PRNU) correction), lens-falloff correction, and dark signal nonuniformity correction (DSNU). The image noise can be estimated based on the signal-to-noise ratio (SNR).

2.2.2 Uncertainty of the reflectance transformation

The rigorous, physical model for the reflectance transformation is given in (2), and our ultimate objective is to develop an error propagation method for this model. In this investigation, we limit our consideration to the simple case of an empirical line-based method as described in section 4.3. In typical situations, we have an overdetermination in our estimation process, and then we can use the least squares (LS) method to calculate the model parameters and their standard deviations.

2.2.3 Implementation of the uncertainty estimation

The reflectance uncertainty estimation can be efficiently implemented in the reflectance calculation process so that an uncertainty value is provided for each calculated reflectance value. When generating reflectance image mosaics, the uncertainty estimates can be stored as images that cover the same spatial area as the image mosaic.

3 Traceable Reflectance Reference for UAV Remote Sensing Campaigns

Our procedure is based on traceable reflectance reference panels that are distributed in the area of interest. This procedure requires targets with well-behaving reflectance properties (Pagnutti et al. 2002) and traceable measurements of the reflectance characteristics.

3.1 *Targets*

A set of dark and bright targets were selected based on our analysis of the BRFs of several targets that were measured in the FGI laboratory using a FIGIFIGO goniospectrometer. The following targets were selected (Fig. 2):

- Field Spectralon: a white Spectralon reference panel 25 cm by 25 cm in size, with a reflectance of 0.99 @ 540 nm (not shown in Fig. 2).

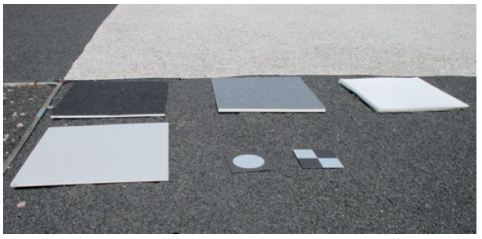

Fig. 2: Traceable reflectance panels 1m² in size. Top row: black carpet (BC) and gray carpet (GC) panels and PTFE90. Bottom row: painted grey panel (GP).

- PTFE90: a white Polytetrafluoroethylene (PTFE) panel 1 m by 1 m in size, with a reflectance of 0.90 @ 540 nm.
- 12 light grey painted panels, 1 m by 1 m in size, with a reflectance of 0.53 @ 540 nm (referred to as GP1 to GP12).
- 2 dark grey panels made of grey carpet, 1 m by 1 m in size, with a reflectance of 0.10 @ 540 nm (GC1, GC2). The carpet has a grooved surface, which might cause some directional influences.
- 2 black panels made of black carpet, 1 m by 1 m in size, with a reflectance of 0.03 @ 540 nm (BC1, BC2). The carpet has a grooved surface.

3.2 *Laboratory Measurements of Reflectance Targets*

A measurement procedure was developed to provide traceability of the BRF measurements done at the FGI for the national standards laboratory at Aalto University's Metrology Research Institute (Nevas et al. 2004). Then traceable BRFs of all the field targets were measured at the FGI laboratory using the FIGIFIGO goniospectrometer (Suomalainen et al. 2009) as follows:

- BRF of all the panels with one illumination angle (50° from zenith);
- BRF of one grey and one black carpet panel with 0°, 45°, and 90° rotation azimuth angles of the panel relative to the illumination direction;
- BRF of one grey painted panel, one black carpet and one grey carpet with two additional illumination angles (40° and 60° from zenith).

From this dataset, and with proper model fitting and interpolation, we can acquire the laboratory BRF of the targets with any illumination zenith angle between 40° and 60°, any viewing zenith angle between -70° and +70°, and any illumination and viewing azimuths freely from a full 360°.

For the grey painted panels, the results from the laboratory measurements showed that the standard deviation of reflectance for the 12 different panels was between 0.004 and 0.006 in reflectance units.

The carpets showed some directional dependency due to their grooved surfaces. For the black carpet, the maximum standard deviation of measurements when rotating the panel 0°, 45°, and 90° (azimuth angles relative to the illumination direction) was less than 0.002; for the grey carpet the corresponding value was 0.01 or less.

We concluded that the estimated standard deviation was 0.006 for the grey painted panels and black carpet, and 0.01 for the grey carpet.

4 Empirical Study

4.1 *Test Site and Ground Truth*

The procedure was evaluated at the FGI's Sjökulla remote sensing test field, located in southern Finland (60.242064 N, 24.383585 E) (Honkavaara et al. 2008). The area is covered with permanent gravel reflectance targets, permanent spatial resolution targets, and gravel field for portable targets. There is no veg-

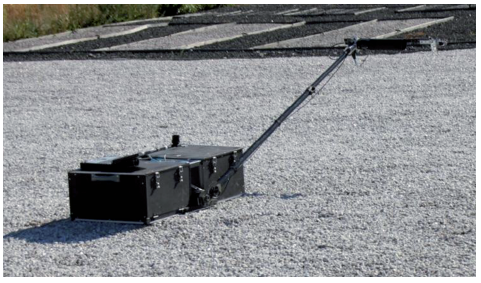

Fig. 3: The FIGIFIGO goniospectrometer measuring white gravel at the Sjökulla test field.

etation in the area (only some random weeds), and the area is practically flat.

All of the reflectance reference targets were distributed in the area. We measured the BRFs of the white, grey and black gravels and one GP panel using the FIGIFIGO goniospectrometer (Fig. 3) for reference.

A total of 85 ground control points (GCPs) with a positional uncertainty of 5 cm were available in the area; for georeferencing 19 GCPs were used. We also had a DSM with a point distance of 10 cm covering the area of interest; its estimated height uncertainty was 6 cm.

4.2 *Image Collection using UAV*

We used an eight-rotor UAV, which was based on MikroKopter autopilot and Droidworx AD-8 extended frame having a 1.5 kg payload (Fig. 4). The UAV was equipped with a stabilized camera mount, the AV130 (Photo-Higher, New Zealand), which compensates for tilts and vibrations around the roll and pitch directions.

The predominant instrument used for UAV reflectance measurements is the Fabry-Perot Interferometer-based (FPI) spectrometric camera, developed by the VTT Technology Research Center in Finland (Saari et al. 2013). This technology provides area-format spectral data cubes, but each band in the data cube has a slightly different position and orientation because they are exposed sequentially. Furthermore, the technology allows for stereoscopic and multi-ray views of objects when overlapping images are used, and an even larger range of observation angles can be obtained by using oblique views.

Fig. 4: MikroKopter UAV (top) and FPI camera (bottom).

The campaign with the FPI spectral camera took place on August 6, 2013 between 10:35 a.m. and 10:44 a.m. local time (UTC +3). The weather conditions were cloud free, providing a stable illumination level and a low level of diffuse illumination; the solar zenith angle was 53° and the solar azimuth angle was 126º.

The FPI image block consisted of two crossing, bidirectional flight lines with an oblique viewing geometry and three flight lines with a vertical viewing geometry (Fig. 5a). There were altogether 62 images. In the vertical block, the forward overlap was approximately 60% and the side overlap was approximately 50%. For the FPI camera images, the FOV was $< \pm 16°$ in the flight direction, $< \pm 27°$ in the cross-flight direction, and $< \pm 31°$ the format corner. We tilted the camera's optical axis around the axis perpendicular to the flight direction (the roll axis) using an oblique angle of 25°–30°. This provided maximum viewing angles of approximately 40° in the flight direction when the border areas of the images are not used; the rotation angles in the image block (roll, pitch, and yaw) are shown in Fig. 5b.

The flying height was approximately 40 m, which provided a ground sample distance (GSD) of 4 cm; the flight speed was approximately 4 m/s. Due to the sequential exposure of the spectral bands, the time difference between temporally adjacent bands was 75 ms, which led to a distance of 30 cm of the perspective centres. It took 1.725 s to collect a single data cube, which resulted in a spatial movement of 7.4 m (29% of the image size in the flight direction). The selected camera settings provided a total of 35 useful spectral bands in the range of 500 nm – 900 nm, with a full width of half maximum (FWHM)

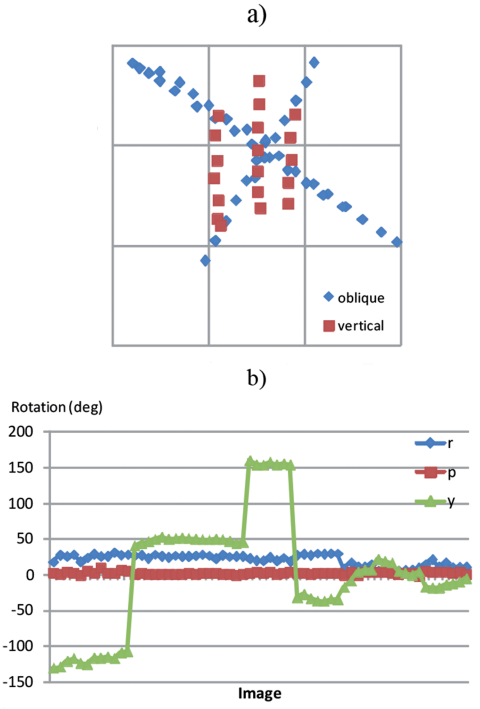

Fig. 5: a) The FPI image block with two bi-directional, oblique crossing flight lines and three vertical flight lines. b) The rotation angles roll (r), pitch (p), and yaw (y) of the images.

between 12.2 nm and 32.2 nm, on average 21.9 nm; the bands can be freely selected with one nm interval (for details, see Honkavaara et al. 2013). For further analysis, we used three bands: (central wavelength; FWHM) band 9 (534.6 nm, 30.2 nm), band 22 (634.9 nm, 16.9 nm), and band 37 (789.4 nm, 27.9 nm).

4.3 *Image Data Processing*

The image processing chain includes image corrections based on laboratory calibrations, band matching of individual bands in the spectral data cube, determination of orientations, DSM generation, atmospheric correction, and reflectance data generation. The methods used to process the FPI spectral camera data mainly consisted of generic methods for processing camera images; only the image preprocessing and band matching phases required some extra sensor-specific steps. The entire processing chain for the FPI camera was developed by Honkavaara et al. (2013).

For this investigation, a simple radiometric processing approach was used in order to better focus on our major research objective, uncertainty propagation in image processing. The model for the reflectance transformation was

$$R = (DN/a_{rel} - b_{abs})/a_{abs}. \quad (6)$$

Parameters a_{abs} and b_{abs} were estimated for one image (a reference image) located in the central area of the block using linear regression. The variable a_{rel} includes the relative parameters of each image with respect to the reference image. We carried out the processing with and without this variable. We either estimated a_{rel} by using the reflectance panels or else we used the radiometric block adjustment method presented by Honkavaara et al. (2012, 2013). Feasibility and the limitations of the model can be considered in different conditions when comparing it to the rigorous model in (1). The method requires a minimum of two reflectance reference panels.

For this model, the estimated standard deviation of the output reflectance is as follows (see (5)):

$$\sigma_R^2 = \sigma_{DN}^2/(a_{rel}a_{abs})^2 + DN^2/(a_{rel}^4 a_{abs}^2)\,\sigma_{arel}^2 + (DN^2/(a_{rel}^2 a_{abs}^4) - 2DNb_{abs}/(a_{rel}a_{abs}^4) + b_{abs}^2/a_{abs}^4)\,\sigma_{aabs}^2 + (1/a_{abs})^2\,\sigma_{babs}^2, \quad (7)$$

where σ_{arel}, σ_{aabs}, and σ_{babs} are the standard deviations of the model parameters. We implemented the uncertainty propagation method during the reflectance calculation process so that the uncertainty was estimated for each calculated reflectance value.

For the geometric processing, we used standard photogrammetric techniques (Honkavaara et al. 2013). In order to automate the processing of oblique images, we implemented the Visual Structure-from-Motion (VisualSFM) method proposed by Wu et al. (2011, 2013) for the processing line. This method was used to provide the approximate orientations for the images. The final processing was carried out using a Socet Set 5.5 photogrammetric workstation. We used 19 GCPs

for georeferencing; measuring the GCPs was the only interactive measurement step in the image processing chain.

5 Results

5.1 *Geometric processing*

Accurate georeferencing is a critical step in the process. We carried out the georeferencing for band 37 of the FPI camera. We estimated the orientations of the images and the camera parameters using a self-calibrating bundle block adjustment. The camera parameters and their standard deviations are shown in Tab. 1. After making the block adjustment, the root-mean-square error (RMSE) of residuals for the GCPs was 5.9 cm, 4.6 cm, and 7.3 cm for the FPI images at the X, Y, and Z coordinates. The good block geometry with vertical and oblique images provided good accuracy.

We interpolated the orientations of the other bands based on the trajectory of the reference band using the known time difference between the bands. These orientations are needed to provide view and illumination angles for different bands. For the reflectance orthophoto calculation, we utilized the orientations of the reference band and the bands that were rectified to the geometry of the reference band.

We calculated the viewing angles (zenith and azimuth) for all panels visible on each image based on the image and panel locations. This data, together with the solar illumination angles, was used to acquire reference BRF for each panel on each image from the laboratory FIGIFIGO measurements.

Tab. 1: Camera parameters and their standard deviations, which were obtained from the self-calibrating bundle block adjustment (x0, y0: principal point of autocollimation, f: focal length, k1: the first order radial distortion).

Parameter	Value; standard deviation
x0 (mm; mm)	-0.015; 0.0027
y0 (mm; mm)	0.012; 0.0024
f (mm; mm)	-0.073; 0.0087
k1 (mm/mm^3)	2.7E-3; 7.9E-6

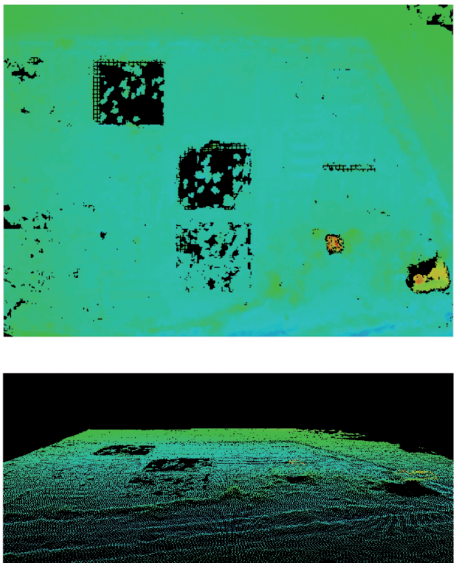

Fig. 6: DSM with a 10 cm point distance measured using automatic image matching and images from FPI camera band 37. The black areas are unsuccessful matches.

We calculated the DSM using the images from FPI band 37. Fig. 6 shows that the automatic matching was not completely successful for the black gravel targets because the SNR was too low. The 84 accurate checkpoints indicated that the RMS error in the DSM was 5 cm, which was a very good result. Because of failures at very dark targets, we used another DSM that was collected using a wide spectral bandwidth, red-green-blue (RGB) camera that provided a sufficient SNR at black targets.

5.2 *SNR*

We calculated the SNR using homogenous reflectance targets (GP1-12, GC1, GC2, BC1, BC2) as the ratio of an average signal to the standard deviation of the signal. We used a window size of 4 by 4 pixels (16 pixels) and we took a median value for all images and targets used. For the GP reflectance panel (reflectance 0.53 @ 540 nm), the SNR was better than 100 in most cases. The SNR was 50 to 100 for the darkest targets (BC) with a reflectance of 0.03 @540 nm. A decrease in the SNR appeared in the NIR bands due to the decreasing quantum

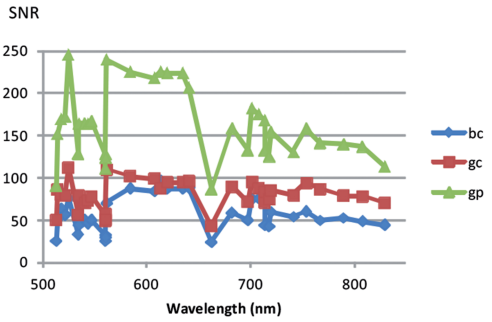

Fig. 7: SNR of the black carpet (BC), grey carpet (GC), and light grey (GP) reflectance panels as the function of the wavelength calculated in an image window 4 by 4 pixels in size.

efficiency of the CMOS image sensor with increasing wavelengths. The edge filters used in the FPI camera limited the spectral bandwidth and decreased the transmission in some of the bands, causing a decrease in the SNRs. Our objective was to ensure that the SNR is greater than 100, which means that the required noise level should be less than 1%; the results were consistent with our expectations. In the following analysis, we used an estimate of $\sigma_{DN} = 0.007$ for the image noise in the reflectance uncertainty propagation.

5.3 *Radiometric Correction*

The first results showed unexpectedly poor accuracy for the radiometric transformation. The analysis indicated that there were systematic radiometric errors in the images. It was not possible to calibrate the camera in laboratory at that point in time, so we estimated a linear correction factor with respect to the darkest corner of the image using an average image for all 62 images. Since the camera observed the object from different directions, the remaining systematic radiometric differences were most likely due to the systematic image errors. This was not a rigorous method, but we decided to use it because it improved the results greatly.

We calculated the empirical line model for one of the images located at the centre of the block with eight reflectance panels; the parameters and their standard deviations are given in Tab. 2. Then, we estimated the relative parameters (a_{rel}) for all other images (Tab. 3); there were in average 5.6 reflectance panels in image. The estimated standard deviations of the radiometric model parameters and DNs were used for the uncertainty propagation (7).

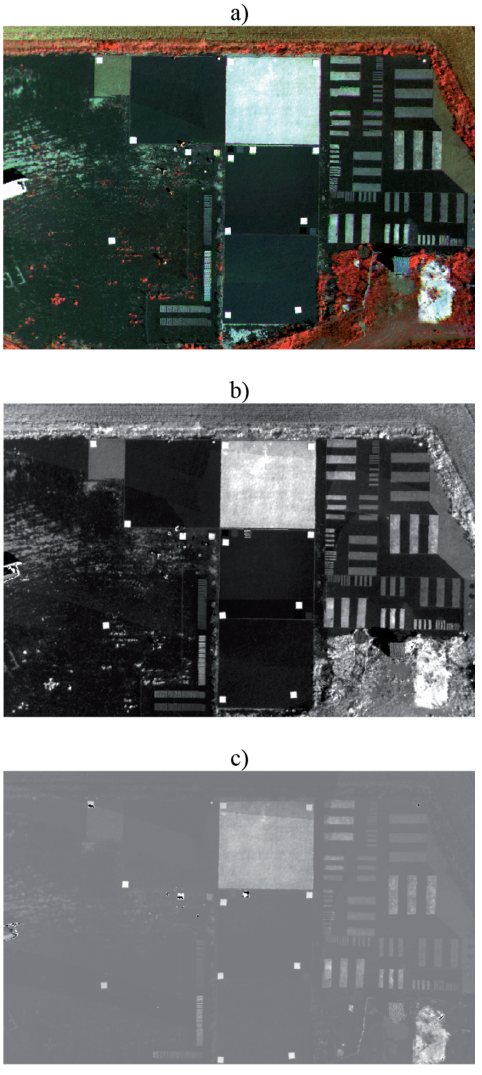

Fig. 8: a) A radiometrically adjusted composite mosaic of bands 37, 22 and 9; b) mosaic of NIR band 37; c) standard deviation plot for reflectance values in b. The maximum standard deviations were for the grey painted panels (nominal reflectance of 0.53) of 0.02–0.025, while the minimum values were for black panels (nominal reflectance 0.03) of 0.012.

Tab. 2: The empirical line parameters and their standard deviations for the reference image for each band (transformation $R = a_{abs}DN + b_{abs}$). a_{abs}, $b_{abs;}$: parameters of empirical line model; σ_{aabs} σ_{babs}: standard deviations of the model.

Band	a_{abs}; σ_{aabs}	b_{abs}; σ_{babs}
9	2.786E-05; 8.427E-07	-0.0102; 0.0120
22	2.93E-05; 9.650E-07	-0.0091; 0.0118
37	3.240E-05; 9.777E-07	-0.0353; 0.0117

Tab. 3: Statistic on the radiometric processing based on reflectance panels: RMSE of standard deviations of relative radiometric parameters (σ_{arel}), RMSE of reflectance residuals for the radiometric transformations (RMSE R), and RMSE of estimated uncertainties for different bands based on error propagation (σ_R).

Band	RMSE σ_{arel}	RMSE R	RMSE σ_R
9	0.023	0.023	0.014
22	0.030	0.028	0.013
37	0.028	0.026	0.015

We generated reflectance orthophoto mosaics using the vertical image blocks. In Fig. 8a, the mosaic is a composite of near-infra-red (NIR), red, and green bands, whereas Fig. 8b shows the mosaic of the NIR band 37. In the orthophoto mosaics, the maximum observation angles were ± 8° in the flight direction and ± 14° in the cross-flight direction. The estimated standard deviation values for Fig. 8b are given in Fig. 8c. Because we did not use the BRDF-model in the mosaic calculation, the estimated standard deviations are accurate only for the isotropic targets. The average estimated standard deviations (σ_R) were 0.013–0.015 for the different bands (Tab. 3, Fig 8c).

5.4 *BRF Extraction*

We extracted BRFs for the various targets from the UAV image block data by using DSM, orientation information, and a radio-

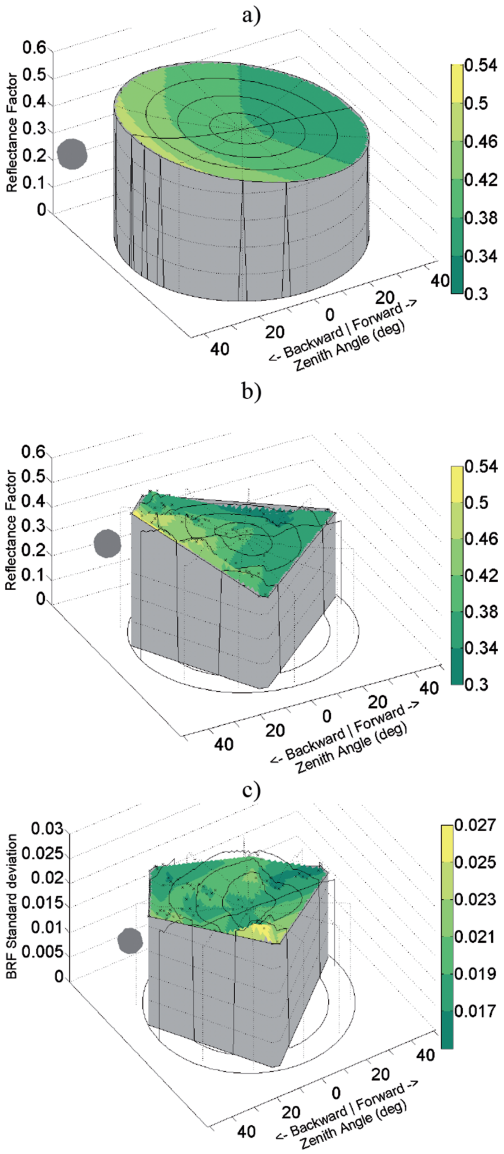

Fig. 9: BRF plot of white gravel at 790 nm measured using a) FIGIFIGO and b) UAV. c) Estimated standard deviation plot for b) based on variance covariance propagation. The illumination angle was approximately 50° above the horizon. The x-axis is the observer zenith angle at the solar principal plane; y-axis is the observer zenith angle at the plane perpendicular to the solar principal plane; z-axis is the BRF. The colour bar indicates the reflectance value (a, b) or standard deviation (c).

metric model. We used BRF observations of a single target, visible on multiple images, to create a BRF plot representing the view-angle dependency of the target. Each reflectance observation was calculated as an average in a 2 m by 2 m area. Strictly speaking, these reflectance plots include also diffuse components; when assuming that the proportion of the diffuse illumination in the clear day was 10% and the difference between the diffuse and bidirectional reflectance was 10%, the uncertainty due to this approximation was 1%, which can be considered as insignificant in this assessment.

As an example, BRF and standard deviation plots for the white gravel (nominal reflectance 0.4) are shown in Fig. 9. Some noise appeared in UAV BRF the plots (Fig. 9b). This is due to the remaining radiometric differences in the images. Nevertheless, the BRF estimates obtained when using the UAV approximated well the more accurate BRFs measured when using the FIGIFIGO (Fig. 9a). Similar conclusions could be made about the black and grey gravel. RMSEs of the estimated standard deviations based on uncertainty propagation were 0.020 for the white gravel and 0.011 for the black gravel (Fig. 9c). In the extracted data, the viewing angles were approximately 40° or less. A wider range of observation angles could be obtained by using higher oblique view angles. To provide denser BRF measurements, more flight directions could be used in the data collection in the future.

6 Discussion

UAVs offer attractive possibilities for measuring the reflectance properties of objects. We have developed a UAV system for BRF measurements that is based on a light-weight spectrometric camera collecting area-format spectral data cubes in vertical and oblique viewing directions. In this investigation, we developed an uncertainty propagation method for image processing that provides uncertainty estimates for the extracted reflectance.

Our investigation included many new aspects. 1) We used a new type of spectrometric camera to measure the spectral reflectance. Ultimately, this system is capable of measuring 3D points and their spectral characteristics. In this way, it offers an excellent possibility for controlled measurements and for rigorous characterization of the object properties. 2) Our method is based on rigorous photogrammetric techniques, which make automated and reliable procedures possible. 3) Finally, the uncertainty propagation method implemented for the processing line is a new idea in UAV remote sensing.

The image processing method has excellent automation potential. In our previous process, a bottleneck occurred when determining the approximate orientations of the images (Honkavaara et al. 2013). The implemented VisualSFM-based method (Wu et al. 2011, 2013) proved capable of automatically orienting image blocks consisting of oblique and vertical images. A further improvement will involve utilizing high-quality GPS information to support the georeferencing process.

Our reflectance transformation procedure is based on traceable reflectance panels. It is a quite laborious process; therefore, methods based on irradiance measurements on the ground and UAV should be further developed for operational applications to minimize the need for field work (Hakala et al. 2013, Burkart et al. 2014). On the other hand, the method with reflectance panels can also be considered as a portable UAV calibration test site that can be used to calibrate and validate various correction methods in different environments.

The results described in this article were preliminary and some sources of uncertainty still remain. 1) The camera calibration appeared to be inaccurate; we estimated the correction factors for the images based on the campaign image data, which caused some uncertainty in the results. 2) The diffuse light from the area surrounding the measurement site and the sky were not taken into account; this caused some inaccuracy in the BRFs. 3) The BRFs measured in the laboratory were used as a reference. In the future, we will investigate integrating the laboratory BRFs with the nadir field reflectance measurements to match the BRFs more accurate to the actual imaging conditions. This method was presented in a study by Markelin et al. (2012). 4) We assumed that the geometric measure-

ments could be considered error-free. We noticed that some discrepancies occasionally appeared, and this might have caused some minor deterioration in the level of accuracy. 5) We used a very simple approach for the reflectance transformation (6); however the developed uncertainty propagation method is a general framework and it can also be used with any reflectance transformation model. Also, further analysis of the object characteristics can be integrated with the uncertainty estimation process. 6) We used only three bands out of 35 available spectral bands. In principle, the same procedures can be repeated for other bands as well.

The measurement setup in local-area UAV applications falls between the conventional methods based on goniometric methods and airborne methods. The methodology can be further improved by adopting many of the best practices from conventional goniometric measurements (Demircan et al. 2000, Schopfer et al. 2008, Suomalainen et al. 2009) as well as from airborne measurements (Richter & Schläpfer 2002). Recently, several new ideas have been presented for UAV radiometric correction, such as downwelling and upwelling irradiance measurements in the UAV and ground (Hakala et al. 2013, Burkart et al. 2014). In the future, we will use these methods to improve our processing line.

We demonstrated the new measurement procedure in an artificial environment with gravels and reflectance panels. In our further evaluations, we will consider the method in more natural environments: in agricultural fields and in the forest.

In this investigation, the major uncertainty components in the reflectance measurement were the uncertainty of the reflectance transformation and the image quality; we assumed that the geometric processing of the measurement system was accurate and did not cause any further uncertainty. The uncertainty of the output is highly dependent upon the atmospheric conditions and camera settings (SNR). In particular, the quality of the radiometric calibration of the sensor is a fundamental factor influencing the uncertainty. With airborne hyperspectral sensors, great effort has been spent in developing accurate calibration procedures (Gege et al. 2009); with UAV camera systems, accurate radiometric calibration methods will be of importance as well (Buettner & Roeser 2014).

The overall objective for the output reflectance data quality was between 0.01 and 0.02 reflectance units; this would meet the requirements of the satellite community for global radiation budget measurements (MetEOC 2013). Our theoretical results indicated that this level of accuracy could be obtained with the proposed method. Also the empirical results were promising. However, the previously mentioned uncertainties in processing likely increased the level of uncertainty somewhat in reality. We expect that significant improvement will be made with an improved camera calibration. We will continue making the improvements for the processing method in order to improve the level of accuracy and automation, as suggested above.

7 Conclusions

We are developing SI-traceable image processing methods for UAV remote sensing. The objective is to establish the uncertainty budget of the reflectance measurements done by the FGI so that they are traceable to the reference measurements of the Metrology Research Institute at Aalto University, which serves as the Finnish national standards laboratory in optical quantities. We have implemented a method that is based on traceable reflectance panels and a traceable Spectralon. This investigation focused on the uncertainty involved in image processing. The uncertainties are propagated via image processing to provide estimates of the uncertainty of the reflectance measurements. We think that developing methods to provide reflectance data using UAV imagery and a rigorous assessment of the measurement uncertainty will be of great importance for many future UAV remote sensing applications.

Acknowledgements

We are grateful to the European Metrology Research Program (EMRP) for funding the project. The EMRP is jointly funded by the

EMRP participating countries that are part of the European Association of National Metrology Institutes and the European Union. This project is part of a Researcher Excellence Grant project, which in turn falls under the EMRP project "Metrology for Earth Observation and Climate". We acknowledge the Metrology Research Institute at Aalto University for their support in providing reflectance standard for our investigation.

References

BIPM, 2004: Web-pages of Bureau International des Poids et Mesures. – http://www.bipm.org/en/convention/wmd/2004/ (8.3.2014).

BUETTNER, A. & ROESER, H.P., 2014: Hyperspectral Remote Sensing with the UAS "Stuttgarter Adler" – System Setup, Calibration and First Results. – PFG – Photogrammetrie, Fernerkundung, Geoinformation **2014** (4), in press.

BURKART, A., COGLIATI, S., SCHICKLING, A. & RASCHER, U., 2014: A Novel UAV-Based Ultra-Light Weight Spectrometer for Field Spectroscopy. – IEEE Sensors Journal **14** (1): 62–67.

DEMIRCAN, A., SCHUSTER, R., RADKE, M., SCHÖNERMARK, M. & RÖSER, H.P., 2000: Use of a wide angle CCD line camera for BRDF measurements. – Infrared Physics & Technology **41** (1): 11–19.

GEGE, P., FRIES, J., HASCHBERGER, P., SCHÖTZ, P., SCHWARZER, H., STROBL, P., SUHR, B., ULBRICH, G. & VREELING, W.J., 2009: Calibration facility for airborne imaging spectrometers. – ISPRS Journal of Photogrammetry & Remote Sensing **64** (2009): 387–397.

GRENZDÖRFFER, G.J. & NIEMEYER, F., 2011: UAV based BRDF-measurements of agricultural surfaces with PFIFFIKUS. – International Archives of the Photogrammetry, Remote Sensing and Spatial Information Sciences **38** (1/C22).

HAKALA, T., SUOMALAINEN, J. & PELTONIEMI, J.I., 2010: Acquisition of Bidirectional Reflectance Factor Dataset Using a Micro Unmanned Aerial Vehicle and a Consumer Camera. – Remote Sensing **2** (3): 819–832.

HAKALA, T., HONKAVAARA, E., SAARI, H., MÄKYNEN, J., KAIVOSOJA, J., PESONEN, L. & PÖLÖNEN, I., 2013: Spectral imaging from UAVs under varying illumination conditions. – International Archives of the Photogrammetry, Remote Sensing and Spatial Information Sciences **40** (1/W2): 189–194.

HONKAVAARA, E., PELTONIEMI, J., AHOKAS, E., KUITTINEN, R., HYYPPÄ, J., JAAKKOLA, J., KAARTINEN, H., MARKELIN, L., NURMINEN, K. & SUOMALAINEN, J., 2008: A permanent test field for digital photogrammetric systems. – Photogrammetric Engineering & Remote Sensing **74** (1): 95–106.

HONKAVAARA, E., HAKALA, T., SAARI, H., MARKELIN, L., MÄKYNEN, J. & ROSNELL, T., 2012: A process for radiometric correction of UAV image blocks. – PFG – Photogrammetrie, Fernerkundung, Geoinformation **2012** (2): 115–127.

HONKAVAARA, E., SAARI, H., KAIVOSOJA, J., PÖLÖNEN, I., HAKALA, T., LITKEY, P., MÄKYNEN, J. & PESONEN, L., 2013: Processing and Assessment of Spectrometric, Stereoscopic Imagery Collected Using a Lightweight UAV Spectral Camera for Precision Agriculture. – Remote Sensing **5** (10): 5006–5039.

HRUSKA, R., MITCHELL, J., ANDERSON, M. & GLENN, N.F., 2012: Radiometric and geometric analysis of hyperspectral imagery acquired from an unmanned aerial vehicle. – Remote Sensing **4** (9): 2736–2752.

HUENI, A., JEHLE, M., DAMM, A., BURKART, A. & SCHAEPMAN, M., 2013: Spectroscopy Information Systems for Earth System Science. – ESA PV2013 Workshop, Frascati, Italy.

MARKELIN, L., HONKAVAARA, E., SCHLÄPFER, D., BOVET, S. & KORPELA, I., 2012: Assessment of radiometric correction methods for ADS40 imagery. – PFG – Photogrammetrie, Fernerkundung, Geoinformation **2012** (3): 251–266.

MetEOC, 2013: Web-pages of the MetEOC – European Metrology for Earth Observation and Climate. – http://www.emceoc.org/ (8.3.2014).

MIKHAIL, E., 1976: Observations and Least Squares. – IEO: 497 p., A Dun-Donnelly Publisher, New York, NY, USA.

NEVAS, S., MANOOCHERI, F. & IKONEN, E., 2004: Gonioreflectometer for measuring spectral diffuse reflectance. – Applied Optics **43** (35): 6391–6399.

PAGNUTTI, M., HOLEKAMP, K., RYAN, R., BLONSKI, S., SELLERS, R., DAVIS, B. & ZANONI, V., 2002: Measurement sets and sites commonly used for characterizations. – International Archives of Photogrammetry, Remote Sensing and Spatial Information Sciences **34** (1): 6 pages.

RICHTER, R. & SCHLÄPFER, D., 2002: Geo-atmospheric processing of airborne imaging spectrometry data. Part 2: atmospheric/topographic correction. – International Journal of Remote Sensing **23** (13): 2631–2649.

SAARI, H., PÖLÖNEN, I., SALO, H., HONKAVAARA, E., HAKALA, T., HOLMLUND, C., MÄKYNEN, J., MANNILA, R., ANTILA, T. & AKUJÄRVI, A., 2013: Miniaturized hyperspectral imager calibration and

UAV flight campaigns. – SPIE 8889, Sensors, Systems, and Next-Generation Satellites XVII.

Sandau, R., 2010: Digital airborne camera – Introduction and technology: 343 pages, Springer Science+Business Media.

Schaepman-Strub, G., Schaepman, M.E., Painter, T.H., Dangel, S. & Martonchik, J.V., 2006: Reflectance quantities in optical remote sensing – definitions and case studies. – Remote Sensing of Environment **103** (1): 27–42.

Schopfer, J., Dangel, S., Kneubühler, M. & Itten, K.I., 2008: The Improved Dual-view Field Goniometer System FIGOS. – Sensors **8** (8): 5120–5140.

Schowengerdt, R.A., 2007: Remote Sensing, Models and Methods for Image Processing. – Third edition, Academic Press Inc., San Diego, CA, USA.

Schwarzbach, M., Putze, U., Kirchgaessner, U. & v. Schoenermark, M.V., 2009: Acquisition of High Quality Remote Sensing Data Using a UAV controlled by an open source autopilot. – ASME 2009 International Design Engineering Technical Conferences & Computers and Information in Engineering Conference IDETC/CIE 2009, San Diego, CA, USA.

Suomalainen, J., Hakala, T., Peltoniemi, J. & Puttonen, E., 2009: Polarised Multiangular Reflectance Measurements Using the Finnish Geodetic Institute Field Goniospectrometer. – Sensors **9** (5): 3891–3907.

Wu, C., Agarwal, S., Curless, B. & Seitz, S.M., 2011: Multicore Bundle Adjustment. – IEEE Conference on Computer Vision and Pattern Recognition (CVPR): 3057–3064.

Wu, C., 2013: Towards Linear-time Incremental Structure from Motion. – International Conference in 3D Vision (3DV): 127–134, Seattle, WA, USA.

Zarco-Tejada, P.J., Gonzalez-Dugo, V. & Berni, J.A.J., 2012: Fluorescence, temperature and narrow-band indices acquired from a UAV platform for water stress using a micro-hyperspectral images and a thermal camera. – Remote Sensing of Environment **117:** 322–337.

Address of the Authors:

Dr. Eija Honkavaara, Teemu Hakala, Lauri Markelin & Jouni Peltoniemi, Finnish Geodetic Institute, Geodeetinrinne 2, 02430 Masala, Finland, Tel.: +358-40-192-0835 (Honkavaara), Fax: +358-9-29555200, e-mail: {eija.honkavaara}{teemu.hakala}{lauri.markelin}{jouni.peltoniemi}@fgi.fi

Manuskript eingereicht: Dezember 2013
Angenommen: März 2014

PFG 2014 / 3, 0189–0195
Stuttgart, June 2014

Report

A Method of Evaluating the Internal Precision of Multi-View Stereo Dense Reconstruction, Applied on Parthenon Frieze

Dimitrios Skarlatos, Limassol, Cyprus, Stavroula Kiparissi, Athens, Sofia Theodoridou, Thessaloniki & Dimitrios Pandermalis, Athens, Greece

Keywords: MVS, precision, computer vision, Parthenon frieze

Summary: Recent advances in Structure-from-Motion (SfM) and multi-view stereo (MVS) techniques are getting a lot of attention in the 3D modeling community, as they provide a sophisticated, versatile and rapid way to compute dense 3D point clouds. Many applications in archeology and aerial, surface or underwater surveys have been reported based in the combination of SfM and MVS. In addition, they become more popular and widespread as commercial applications and Internet services are emerging. Nevertheless, there is no known way to evaluate the precision of the extracted point cloud. This paper presents a method for estimating the precision of each point in the final point cloud generated by open source MVS, as it is applied to the Parthenon frieze in the Acropolis Museum.

Zusammenfassung: *Methode zur Bewertung der internen Genauigkeit einer Dense-Stereo-Messung, dargestellt am Parthenonfries.* Die neueren Entwicklungen bei Structure-from-Motion (SfM) und multi-view stereo (MVS) sind von großem Interesse, weil sie eine differenzierte, praktische und schnelle Methode zur Erzeugung von 3D-Punktwolken darstellen. Man findet viele Anwendungen, z.B. in der Archäologie und bei der Datenerfassung aus der Luft, auf dem Boden und unter Wasser. Verstärkt wird die Entwicklung durch die vielen neuen kommerziellen Lösungen, aber auch die freien Angebote, besonders im Internet. Es fehlen aber noch allgemein anerkannte Methoden zur Bewertung der Genauigkeit der erzeugten Punktwolke. Dieser Artikel stellt eine Methode zur Bestimmung der Genauigkeit jedes einzelnen Punktes einer Punktwolke vor, die mit MVS erzeugt wurde. Der Datensatz wurde am Parthenonfries gewonnen.

1 Introduction

Computer vision lacks a solid definition, as it endorses many subjects, among which 3D reconstruction algorithms hold a prominent position. Such algorithms, focusing on the domain of machine vision, advanced quickly starting from zero, using linear models as mathematical background. Most of them were developed for speed and real time processing rather than metric accuracy (Szeliski 2011). It soon become apparent that photogrammetry could be benefited by computer vision algorithms or vice versa. Nowadays, image based modelling (IBM) emerges as a separate branch in computer vision involving algorithms for Structure-from-Motion (SfM) and multi-view stereo (MVS). Many applications were reported using IBM to record archaeological sites or objects, using open source or commercial software. Nevertheless, there is no report on the estimation of the precision of IBM, while this method is widely adopted by experts and non-experts in a variety for applications from simple shape capturing up to 3D printing reconstruction. Addressing both non-experts to help them avoid misleading results and overestimating technology, as well as experts who

www.schweizerbart.de
DOI: 10.1127/1432-8364/2014/0219
1432-8364/14/0219 $ 2.00

wish to evaluate results, this paper introduces a method to estimate precision of a point cloud generated using SfM and MVS methodology, so that users may have an estimation of their results. The developed method was applied to 3D point clouds of Parthenon Frieze marble blocks, as this work was a part of the "Digitization, renovation and reconstruction of the Parthenon frieze and offerings" research project, where the precise three-dimensional modeling of Parthenon frieze within an accuracy of some tens of microns was required.

As Parthenon's frieze is a unique world document, which lasted the test of time, many 3D recording attempts have been made in previous years. Attempts have been made to digitally reunify all marbles (Stumpfel et al. 2003) using structured light scanning. The project was involving scanning of all marbles hence the adopted method was focused on productivity, speed, flexibility and resolution of about 1 mm. Remondino et al. (2008) have adopted IBM methods, mostly multi image matching, to produce a 3D model of the Erechtheion temple in Acropolis. Attempts using laser scanners report on the density of points and the accuracy of the model based on the scanner's specifications data sheet. While this as a fact is arguable, the precision on points depends on scanner-object distance as well as other factors which are different for each point. Reports using IBM mention an accuracy based on the block adjustment figures and on the sensor pixel size, while in the case of a scanner many more factors affect the final precision. Nevertheless, none of them, laser scanning or IBM, has metadata information about the accuracy of the model or the raw data (points) themselves.

In this study, the quality of the point cloud was of most importance and the highest possible precision was required. Therefore, the proposed method was developed to estimate the precision of each point of the point cloud using standard photogrammetric techniques. The method reads Bundler (Snavely et al. 2007) and patched based multi-view stereo (PMVS) (Furukawa et al. 2010) geometry output files to calculate the precision of all rays intersection, from images to the point, using least-squares (LSQ) estimation.

2 Methodology

2.1 *Tools*

When the project started, November 2011, the open source Bundler followed by CMVS/PMVS work flow were available (CMVS = clustering views for MVS). The combination of Bundler and CMVS/PMVS allows the processing of huge sets of random photographs, taken with uncalibrated cameras to produce a dense 3D colour point cloud, with arbitrary scale. The latter was recovered within Geomagic software using scale bar measurements. During the photo-takes, scale bars were placed above and below the marble block, thus they were reconstructed in the final point cloud. In order to compute a single scale factor, multiple 3D distance measurements were taken and the mean scale factor was applied to the point cloud. The photo acquisition process is very important as it ensures multi photo coverage of the object, undercut visibility and density of the point cloud. Differences in scale and rotations of the photos were subtle enough to be recovered using Bundler in our implementation. Bundler is a rather black box operation, which does not provide much functionality while CMVS\PMVS, which were used for dense multi image matching, allow for a number of parameters to be selected so that the user can set and adjust processing with respect to object's needs. Among these factors are the density of the collected points in terms of pixels on the photos, the minimum number of images on which the point must be visible to be accepted and the patch template size.

2.2 *Application of Analytical LSQ Model*

The main principle for computing 3D points behind both traditional photogrammetry and MVS algorithms is the same and is well known as stereo triangulation. The 3D location of each point is estimated by modern MVS algorithms as the optimal intersection of multiple pairs of optical rays. Thus, the final position is influenced by errors due to many factors, such as the quality of camera calibration, external orientation parameters of the

photos, the image matching quality, the number and geometry of the line intersections in 3D space. Not all of these factors were available through the Bundler and PMVS exported files and therefore estimations had to be made to formulate the design and weight matrices of the least squares. For each reconstructed point, the mean value of the correlation coefficients of all matched projections, is calculated and available in PMVS log file. This value is an indication of how well this point is matched across the images, thus is a good quality indicator which can be used to weight image observations. Low correlation scores indicate areas with no texture, occlusions or strong angles; hence the 2D imprecise measurement will affect the final 3D point localization. For each point the mean correlation value was used as the element of the diagonal of the weight matrix (**W**). Note that the use of different correlation values for each point correspondence would be more appropriate, unfortunately such information was not available.

The camera calibration quality and network geometry of cameras viewpoints, also affect the final precision. The principal point and distortion coefficients affect the precision of point 2D measurements, while focal length error affects the scale factor. Small errors in the latter may be absorbed by the block adjustment, especially if all photos are treated as being taken by separate cameras. By default Bundler treats all photos as they were taken by different cameras, hence automatically calibrates all of them. Since all photos were taken in auto focus mode in order to avoid unfocused images due to variations in the object distance, the Frieze's strong relief and different viewing angles, a different focal length value was computed for each one of the images. The parameters and the accuracy of the exterior orientation of the photos contribute to the final point cloud accuracy as well. 3D positions computed from the intersection of optical rays with a short base may suffer from those errors. Unfortunately, there is no information about the exterior orientation parameters within the Bundler files, hence there is no way to extract meaningful information for **W**. However, even if such accuracy information is not involved in the precision estimation, the values of the above mentioned interior orientation parameters are. Thus, the network geometry is taken into consideration for the computation of the σ_X, σ_Y, σ_Z values. Finally one single overall accuracy value is computed as the length of a 3D error vector.

The method is fully automated and the only value given by the user is the scale factor of the point cloud, so that precision values are converted in real world units. In particular, the input data of the algorithm are: exterior orientation parameters of all images and their focal length, which are included in the output file of Bundler, the 3D point cloud in the ply-format, a scale factor and additional information about 3D points such as the number of images where each point was visible and the mean correlation coefficient for each point included in the PMVS output patch-file. For each 3D point, the algorithm collects all the information needed and computes an error value as described above. The new ply-file of the original point cloud is exported, where an extra column with the quality measure is added. After that, a filtering approach is applied and all points with an error lower than $2\sigma_o$ are excluded. In both stages, before and after the removal of outliers, statistics are computed. For the visualization of the results the open source software CloudCompare was used.

3 Applications

In the context of this work, the Bundler – PMVS pipeline was applied to original marble blocks of the Parthenon Frieze, exhibited in the Acropolis Museum. Before applying the precision evaluation algorithm to an entire block, it was crucial the method be validated in a smaller dataset under controlled conditions, in order to check whether the absence of focal length and exterior orientation standard deviations affect the proposed mathematical model. For this reason a small part of the second marble block from the North Frieze (NF II) was used. After this initial test, a dense point cloud of the sixth marble block from the East Frieze (EF VI) was generated and its precision was estimated using the developed method.

3.1 *Verification*

The aim of this test was the validation of the proposed algorithm. Thus the relative precision among controlled datasets was compared. It was expected that the use of more photos and a higher image resolution should improve the precision. A part of the NF II marble block has been used as a test area, forming the TST dataset. Twelve vertical photos (Fig. 1) were taken with a full frame Canon 6D camera (5472 × 3648 pixels, 36 mm × 24 mm CMOS, 6.55 µm pixels size) with a fixed 50 mm lens, from a distance of approximately 1 m.

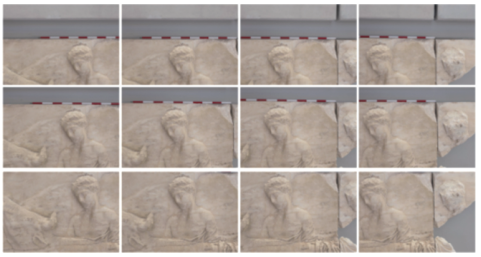

Fig. 1: The TST image dataset.

Using the Bundler output, four point clouds were extracted with different PMVS parameters. The pixel size varied, using the levels 1 and 2, with a minimum of two or four images for the extraction of the point cloud. The latter means that all points which can be correlated in at least two or four photos will be recorded of the final point cloud. The value two means that in the final point cloud points that were found in 2 or more images will be used for the 3D point computation in the final point cloud. All extracted point clouds were processed with the proposed method for the precision calculation (Tab. 1). From the very beginning advantages of the proposed method became apparent, when correlation failed on the featureless background wall, producing spurious points which should be eliminated to produce a meaningful result. Therefore, noise reduction took place by eliminating points with an error larger than $2\sigma_o$. Visualization results for the raw point clouds are presented in Fig. 2, while statistics over precision estimation after noise reduction are presented in Tab. 1. Observing both Fig. 2 and Tab. 1, it becomes apparent that the proposed method works well, since the results are meeting the expectations. In more detail, the error values show that a multiple intersection with four images is more accurate than the simple case with only two images. The above is presented in Fig. 2, where areas with many overlapping images are marked by colours as higher precision areas. The standard deviation values seem to be stable in the case of multi-view stereo while in the simple case they seem to be correlated to the pixel size. Additionally, the maximum estimated error after noise reduction deteriorates fast with respect to a larger pixel size, while the same measure on multi-view stereo remains stable. Once again multi-view stereo filters outliers internally much better. Finally, it has to be noted that in all scenarios, the largest error values appear in the flat grey featureless area above the marble stone, because in this part the image matching may return wrong correspondences. The fact that PMVS computed 3D points in this area, means that the correlation values were near 1.00, as the texture of two windows may be identical but the windows are still not be the same. The above is an example of outliers that

Tab. 1: Estimated precision on TST dataset. Window size decreases along with subsampling level so that the correlation area remains the same on every test.

pmvs parameters	level	0	0	1	1
	cell size (pix)	2	2	1	1
	window size (pix)	15	15	7	7
	min no of images	2	4	2	4
	no of 3D points x103	1468	1270	1529	1255
filtered	mean σXYZ (mm)	0.385	0.346	0.413	0.346
	std σXYZ (mm)	0.244	0.108	0.315	0.111
	max σXYZ (mm)	3.969	1.056	4.020	1.078

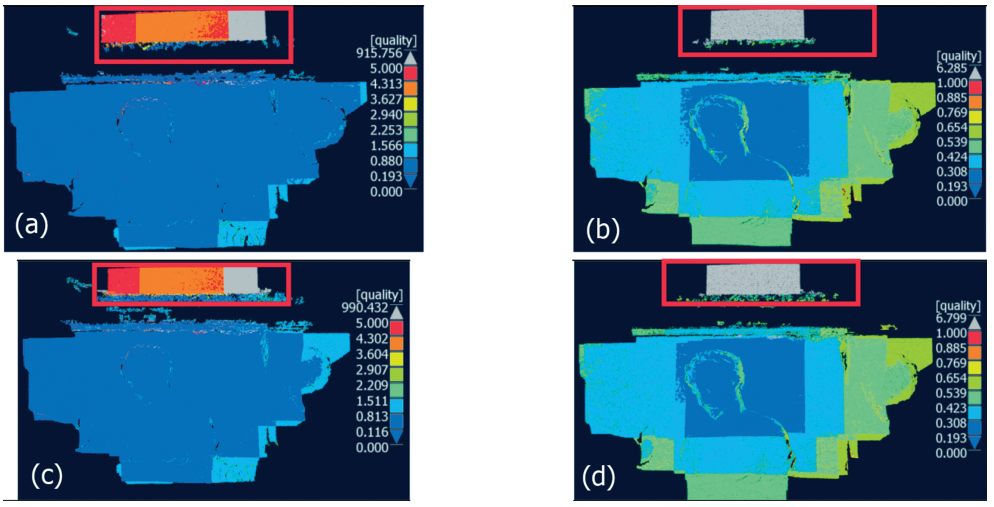

Fig. 2: Visualization results from TST dataset before noise reduction. Marked in red, the wall where correlation fails. a) level 0, min no of images 2, b) level 0, min no of images 4, c) level 1, min no of images 2, d) level 1, min no of images 4.

PMVS failed to filter but the proposed method detects them as uncertain 3D points.

3.2 *Application on a Frieze Block*

EF VI is a long fragmented block and its left part which depicts the gods Poseidon, Apollo and Aphrodite has a length of 1.40 m. This part of carved stone is a well-preserved scene showing the gods cloths with nice sharp folds and many surprising details. During the project a very dense point cloud of this block was generated and the proposed method was used in order to compute its precision. For the 3D digitization, 330 images with convergent geometry were taken with the Canon 6D camera with 50 mm lens, from an average distance of 0.70 m. In order to ensure the adjustment in the processing phase, additional photos were taken from longer distances, i.e. up to 2 m, to act as bridges for the more detailed images. A dense aerial imagery layout was used to ensure full coverage of the marble block. Additional convergent photos were employed from approximately 0.7 m distance and longer to ensure that undercuts would be visible in at least five images. The data acquisition phase is very important to the results of MVS both in terms of final product density, completeness and precision. Although the main guidelines for the block layout are similar to what is known from aerial photography, the solution of undercuts and complex geometry with convergent or oblique photos cannot be defined by strict rules as it is depended on the photographer's experience. Unfortunately, MVS is a post processing technique, so that incomplete areas may reveal afterwards. In this application, the following PMVS parameters were used: image pyramid level 1, cell size 2, window size 7. The final result contained a dense point cloud with 17 million 3D points, corresponding roughly to 20 points per square mm. At a first glance, the resolution of the reconstructed point cloud meets the accuracy and completeness requirements.

4 Results and Conclusions

The proposed method applied to EF VI returns a mean error of 0.193 mm, standard deviation equal to 0.118 mm and maximum error 9.556 mm. In Fig. 3, where the initial error values are visualized, it can be seen that points with such large errors (~ up to 1 mm coloured with red) are very few and that almost the en-

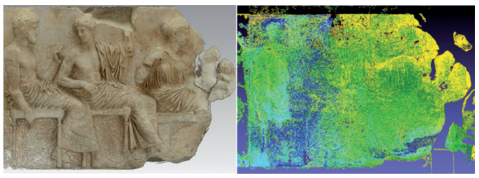

Fig. 3: EF VI point cloud (left) and visualization of precision results before noise reduction (right).

tire model has a precision better than 0.5 mm (points coloured with blue, green and yellow). Fig. 4 shows that 54% of the 3D points have estimated precision of 100 µm – 200 µm, 21% of 50 µm – 100 µm and 20% of 200 µm – 300 µm which means that 90% of the point cloud has a precision between 50 µm and 300 µm, which is acceptable.

In this case, a filtering approach was applied. Once again, points with an error larger than two times the sigma zero were detected and rejected considered as outliers. After this step, error values decreased significantly, especially the maximum. Specifically, the mean error was 0.172 mm, the standard deviation was 0.060 mm and the maximum error fell to 0.658 mm, ensuring that the objective of digitizing Parthenon Frieze at the tens microns level was reached. Note that after the noise reduction no 3D point has an error value over 1 mm. The mean precision has not changed significantly while the fact that the new standard deviation value is equal to 60 µm means that all points enjoy a similar precision and no areas are vastly better or worse.

The proposed precision evaluation method has been tested under controlled conditions and applied to a Parthenon's frieze marble block as a proof of concept. The algorithm does not take into consideration external and internal orientation errors as they were not available. Nevertheless, the proposed model uses all available information about the precision of correlation among images and the geometry of intersected 3D lines in a point to point basis in order to calculate the quality of the extracted point cloud. The final result proved to be an excellent evaluation tool for comparing a number of factors affecting overall precision and accuracy. In the Parthenon frieze project in particular it was used to optimize data acquisition in terms of distance, camera resolution and photo layout, realize strong and weak points of MVS, compare it to the main laser triangulation technique used and calculate overall precision of our modelling techniques and document with metadata information the digital frieze.

Further research should focus on the evaluation and the use of the standard deviation of the external orientation results as well as a better documentation of the 2D precision evaluation, in order to improve the results. The use of external reference data for an overall accuracy estimation and a comparison to precision estimation is also under investigation.

Acknowledgements

This research was supported by the 09SYN-62-629 project "COOPERATION 2009 – Partnerships of Production and Research Institutions in Focused Research and Technology Sectors". The public expenditure is co-

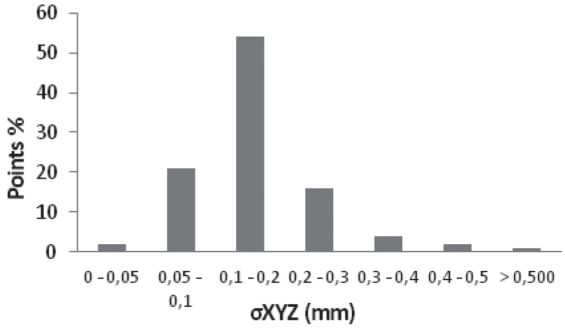

Fig. 4: Estimated precision of EF VI dataset.

financed by the European Regional Development Fund (ERDF) of the European Union and by National Resources. We are grateful to the senior conservators of the Acropolis Museum D. Maraziotis, C. Vassiliadis and others in team. We are also grateful to the Director of the Laboratory for Machine Tools & Manufacturing Engineering in AUTH Prof. Dr.-Ing. habil. Dr.-Ing. E.h. K.-D. Bouzakis.

References

Furukawa, Y., Curless, B., Seitz, S.M. & Szeliski, R., 2010: Towards Internet-scale Multi-view Stereo. – IEEE Conference on Computer Vision and Pattern Recognition: 1434–1441.

Remondino, F., El-Hakim, S., Baltsavias, E., Picard, M. & Grammatikopoulos, L., 2008: Image-based 3D modeling of the Erechteion, Acropolis of Athens. – International Archives of Photogrammetry, Remote Sensing and Spatial Information Sciences **37** (B5): 1083–1091.

Snavely, N., Seitz, S.M. & Szeliski, R., 2007: Modeling the World from Internet Photo Collections. – International Journal of Computer Vision **80** (2): 189–210.

Stumpfel, J., Tchou, C., Yun, N., Martinez, P., Hawkins, T., Jones, A., Emerson, B. & Debevec, P., 2003: Digital reunification of the Parthenon and its sculptures. – 4th International conference on Virtual Reality, Archaeology and Intelligent Cultural Heritage: 41–50.

Szeliski, R., 2011: Computer Vision, Algorithms and applications. Springer.

Addresses of the Authors:

Prof. asst. Dimitrios Skarlatos, M.Sc. Stavroula Kiparissi & M.Sc. Sofia Theodoridou, GeoAnalysis S.A., G. Genimata Str. 54, GR-55134 Thessaloniki, Greece, Tel. +30-231-049-6800, Fax. +30-231-049-6880, e-mail: dimitrios.skarlatos@cut.ac.cy, {skiparissi}{sofia}@geoanalysis.gr

Prof. em. Dimitrios Pandermalis, The Acropolis Museum, Dionysiou Areopagitou Str. 15, GR-11742 Athens, Greece, Tel. +30-210-900-0900, e-mail: presidentsoffice@theacropolismuseum.gr

Manuskript eingereicht: Januar 2014
Angenommen: März 2014

PFG 2014 / 3, 0197–0208
Stuttgart, June 2014

Report

The Assessment of using an Intelligent Algorithm for the Interpolation of Elevation in the DTM Generation

Hossein Bagheri, Tafresh, Saeed Sadeghian, Tehran & Seyyed Yousef Sadjadi, Tafresh, Iran

Keywords: digital elevation model, digital terrain model, ANN, IDW, AI, GA, interpolation, elevations, optimisation, height

Summary: Several methods exist for the interpolation of digital terrain models (DTM), which have different characteristics depending on environmental conditions and input data. In this paper, the artificial intelligent (AI) techniques such as genetic algorithms (GA) and artificial neural networks (ANN) are used on the samples to optimise the interpolation methods and production of digital elevation models (DEM). The results obtained from applying GA and ANN are compared with typical methods of interpolation for the creation of elevations such as Kriging. The results show that AI methods have a high potential in the interpolation of elevations. The use of artificial networks algorithms for the interpolation and optimisation based on the quartic polynomial and inverse distance weighting (IDW) led to high precision elevations.

Zusammenfassung: *Verwendung von Methoden der künstlichen Intelligenz zur Ableitung von Höhenmodellen*. Für die Interpolation von Höhenmodellen gibt es viele Methoden. In diesem Artikel werden Methoden der künstlichen Intelligenz (artificial intelligence, AI) zur Optimierung von digitalen Höhenmodellen vorgestellt. Dazu gehören Genetische Algorithmen (GA) und künstliche neuronale Netze (ANN). Die mit diesen Methoden erzielten Ergebnisse werden bisherigen Verfahren gegenübergestellt, unter anderem dem Kriging. Im Ergebnis zeigt sich, dass die künstliche Intelligenz große Möglichkeiten bietet. Besonders die Quartic Polygone und die "inverse distance weighting"-Methode könnten für die Ableitung von genauen Höhenmodellen verwendet werden.

1 Introduction

Three-dimensional modelling of the Earth is one of the most important tools in various fields of geology, meteorology, civil engineering, environmental engineering, and numerous engineering projects, and it has many applications in geographic information systems (GIS) (Petrie & Kennie 1990, Florinsky 2011, de Mesnard 2013). In GIS, the terrain modelling is generally called digital terrain modelling (DTM) and is used to display topography and synthetic changes of many environmental parameters such as temperature, air pollution, etc. (Kasser & Egels 2002, Li et al. 2004). One of the most significant parameters in GIS is the topography of the Earth, which can be visualised in a 3D digital form to represent the digital elevation model (DEM) (Abdul-Rahman & Pilouk 2008). In other words, DEM continuously displays elevation changes of the Earth surface, which is directly proportional to the plane position (x,y) (Abdul-Rahman & Pilouk 2008, Chaplot et al. 2006, Miller & Laflamme 1958). Initially, 3D models were created physically from plastic, sand, clay, etc. (Li et al. 2004). Today, however, computers are used to display the Earth's continuous surfaces in a digital form (Heesom & Mahdjobi 2001).

One of the most important issues in the field of digital modelling is the generation of a DEM with high quality and precision under minimum costs. To estimate a continuous surface, due to the limited number of samples and the necessity of reproducing altitude points,

www.schweizerbart.de
DOI: 10.1127/1432-8364/2014/0220
1432-8364/14/0220 $ 3.00

mathematical interpolation functions are used to estimate the elevation of midpoints (Abdul-Rahman & Pilouk 2008). Interpolation methods are used to determine unknown altitudes of midpoints from the samples and as a result, the coordinated points are reproduced and the digitally formed Earths' continuous surfaces can be visualised. An interpolation is never exact. The inherent errors may propagate to a level that becomes inacceptable. Such errors transfer inaccurate assessments into the projects and cause the financial losses, and even produce life threatening results (Eyvazi et al. 2007, Mitas & Mitasova 1999). Therefore, one of the challenges in this field is finding an appropriate method for the height interpolation because in addition to the accuracy and distribution of sample points and the geomorphological characteristics of the Earth's surface, the method for the interpolation and the estimation of the average point height will affect the quality and the accuracy of the DEM (Li 1990, Li 1992a).

Numerous methods for the interpolation have been proposed (Hardy 1971, Hardy 1990, Larsson & Fornberg 2005), which show different results influenced by the environment's conditions and data input. Usually, the optimal method of interpolation depends on the root-mean-square error (RMSE) of the output. In most studies the comparison of interpolation methods and the selection of the optimal methods are used to achieve higher accuracy (Yanalak 2003, Amidror 2002, Rees 2000, Yang et al. 2004, Li & Heap 2011, Wagnera et al. 2012).

In this paper, AI techniques such as ANN and GA are examined to optimise the interpolation methods and the creation of DEM on the samples. At the end, the results of the estimated heights from the intelligent techniques and the usual methods of interpolation are compared.

2 Artificial Neural Networks

Artificial neural networks (ANN) are based either on the performance of the human brain and its functionality or actions can be interpreted according to the human conduct. Investigations show that this network has the ability of learning, reminding, forgetting, concluding, pattern-recognition, classification of information and many other brain functions (Hertz et al. 1991). ANN is essentially made up of simple processing units called neurons (Foody et al. 1995). ANN structures are in the form of layers, which consists of an input layer, an output layer and one or more intermediate layers. Each layer contains several neurons that are connected by a network, which has different weights. Based on how the nodes are connected, the ANN is divided into two groups, feed forward ANN and feedback ANN. In the feed forward input applied to produce the output, neurons must be used as the pathway. A feed forward ANN is known as a "perceptron". Perceptron ANN is one of the most important and widely used aspects in diagnosis classification model (Picton 2000). Perceptron can be single-layered or multi-layered. The difference between single-layer and multi-layer perceptrons is the number of hidden layers between the input and the output layer. The task of these hidden layers is the extraction of the non-linear relationships of the input layer.

The two main steps that exist in the application of ANN are learning and recall. The aim of ANN learning is finding the optimal weights of neuron connections, which is achieved by the recursive method (Holland et al. 1989). Generally, the error back propagation learning rules are used to train the multi-layer perceptron ANN. The law of error propagation is composed of two main routes; the first route is called way-in path, where the input vector affects the multi-layer perception (MLP) network and impacts on the output layers through the intermediate layer. The output vector of the output layer is the actual response of the MLP network. In this way, the network parameters are fixed and unchanged. The second route is called the come-back path. In the come-back path, unlike the way-in path, the MLP network parameters can be changed and adjusted. This adjustment is consistent with the error correcting rule. The error signal at the output layer of the network is formed. The error vector is equal to the difference between the desired response and the actual response of the network. In the come-back path, the calculated error values are distributed in the entire network through the network lay-

ers. In this repetitive process, the corrected parameter weights are calculated and will be added to the previous weights and hence modified to prepare for implementation in the network (Wiszniewski 1983). In this algorithm, the network weights are based on the gradient method and the error signals are corrected and adjusted. Back propagation is used for explaining the correction of network behaviour, which is opposite to the weight communication between synapses (Wiszniewski 1983).

3 Genetic Algorithms

In 1960, Rechenberg presented the basic idea of evolutionary algorithms, where GA can be derived from. This is, in fact, a computerised search method, which is based on optimisation algorithms, named genes and chromosomes, developed at the Michigan University by Holland (Holland et al. 1989) and later by Freisleben & Merz (1996).

In this algorithm, due to being derived from nature, stochastic search processes are used for optimisation and learning problems (Sheta & Turabieh 2006). In nature, chromosome combinations will produce a better generation. Mutations occurring among the chromosomes may improve the next generation. GA solves these problems by using this concept (Sivanandam & Deepa 2010).

Overall operations of this algorithm are: fitting, selecting, combining and mutating (Ravagnani et al. 2005). In the algorithm process, an initial population of chromosomes is selected for the creation of a new and possibly better generation. Each chromosome has various arrays that should be optimised. After creating the initial population of merit (cost consumption) for each chromosome in the population the calculation is based on the objective function. The major parts of the costly (expensive) chromosomes are left behind and the cheaper chromosomes are kept to produce the next generation, the children. Among them, there are a number of elite chromosomes, which are considered to be cheap, and therefore remain untouched until the next generation. To determine the number of chromosomes needed for the evolution, parents are selected to produce offspring. Two chromosomes are selected as parents when they are combined. Sometimes genes are changed randomly. A mutation occurs and enables the algorithm to search for a wider area. In other words, a new generation can be created by reproductive processes of combining gene and mutation. This process must be repeated many times to achieve convergence and create an optimal solution (Haupt & Haupt 2004).

4 Height Interpolation Methods

The main purpose of using the known point height interpolation is the determination of the heights of the unknown's middle points. In 2004, Yang examined different methods for the interpolation according to the accuracy and applicability by using Surfer 8.0 software (Yang et al. 2004). These methods can be divided according to different criteria (Abdul-Rahman & Pilouk 2008). For example, interpolation methods based on surface coverage divided into local and global criteria. In the global methods, the height of all control points are used to estimate the heights for the unknown points, but in the local methods, calculation of unknown point heights are derived from the height of the neighbours' points. In this research, the different methods of interpolation are used to estimate the heights at the unknown points within the local methods, which are explained in the following sections.

4.1 *Inverse Distance Weighting Method*

In the inverse distance weighting (IDW) method, the height information of neighbouring points is used as a weight according to the distance to unknown points. Weight is a function of the distance from the unknown point and hence closer points have higher weights. For height calculation, the following equation is used

$$z = \frac{\sum_{i=1}^{n} \frac{zi}{d_i^p}}{\sum_{i=1}^{n} \frac{1}{d_i^p}}. \quad (1)$$

In (1), p is the speed reducer weight control rate according to distance, where it is equal to 2, d_i is the distance from unknown point to a well-known point and z_i represents the height of point i (Lu & Wong 2008, de Mesnard 2013).

4.2 *Polynomial Method*

This method approximates the surface using polynomial terms plain elements x, y in the form of $z = f(x, y)$. The n power of this polynomial equation is

$$z = \sum_{i=0}^{n} \sum_{j=0}^{n} a_{ij} x^i y^j \ . \tag{2}$$

Where x, y are turned parts and plain components of known points and a_{ij} are polynomial coefficients, which are determined using the know elevation values in the sample points and are obtained by least-squares portion.

4.3 *Kriging Method*

The Kriging method was introduced by Matheron (1963), based on the Krige variables theory zone (Krige 1951). This method is estimated based on a weighted moving average due to which the Kriging method of interpolation considers two criterions, the distance and the change of point elevation. It is the best unbiased linear varygram of weights with the minimal estimation of variance. This means that the difference between actual and estimated values is minimal. In the Kriging method, there are numerous techniques for computing the height values, which normally is divided into two different ways, ordinary Kriging and general Kriging. The ordinary Kriging is calculated based on (3):

$$z(x, y) = \sum_{i=1}^{n} \lambda_i z(x_i, y_i) \ . \tag{3}$$

Where z (x, y) is the height estimated at an unknown point, z (x_i, y_i) is the height of a sample point i and λ_i is the weight of point i.

For the estimation of the weight, various varygrams are used such as linear, exponential, Gaussian and spherical. The general Kriging method is also the combination of ordinary Kriging with local process. The local process can be defined in two ways, i.e. linear trend and quadratic.

4.4 *Nearest Neighbour Method*

In the nearest neighbour method, the nearest point to the unknown neighbour is selected and its height assumed based on the height of the unknown point. This method is an appropriate way if the data is taken based on a regular network and matching with the grid lines.

4.5 *Natural Neighbour Method*

The natural neighbour method was developed in 1980 by Sibson (1980). This method is based on a Voronoi Pattern for a set of separated points. A Voronoi Pattern is a diagram, which is dividing space into a number of regions. This method has more advantage compared with the nearest neighbour's method such as its ability to create a surface that is relatively smooth. This method is based on (4) (Sibson 1981):

$$z(x, y) = \sum_{i=1}^{n} \lambda_i z(x_i, y_i) \ . \tag{4}$$

Where z (x, y) is the estimated height at an unknown point, z (x_i, y_i) is height of sample point i and λ_i is the weight of a sample i followed by the area enclosed by any parts of the unknown sample point.

4.6 *Triangulation Method*

This method deals with the linear interpolation elevations based on a Delaunay triangulation (Zhong et al. 2008).

After the surface reconstruction with Delaunay triangles, the unknown height can be determined.

5 Data Assessment and Evaluation Criteria

In order to compare smart and ordinary interpolation methods, two areas are selected. Area 1 has been mapped by the existing software AutoCAD Civil 2D Land Desktop 2009 and area 2 presents new mapping data, 1:2000 in Port Khamir, which is located in Hormozgan State in the southern part of Iran. In both areas, a number of points are used as the control points. Other points are considered as the check points that are grouped in two series of check points and they are called check points type 1 and type 2. The characterizations and number of control points and two series of check points in both areas are shown in the Tabs. 1 and 2. Using control points and interpolation methods, the heights of the two series of check points (1 & 2) are obtained and it is compared with the actual height. Finally, the extent of errors that exist in the calculated elevations through interpolation methods can be determined by using the RMSE rate. The measurement of the RMSE can be expressed as follows:

$$RMSE = \sqrt{\frac{\sum_{i=1}^{n}(z_{comp} - z_{actual})^2}{n-1}}. \quad (5)$$

Where, z_{comp} is the calculated height values and z_{actual} is the actual check point height.

6 Using Neural Networks in Heights Interpolation

The interpolation of elevations based on ANN uses the perceptron network, which consists of three layers, an input layer, an intermediate layer and an output layer. Structure and network topology is shown in Fig. 1. Two neurons in the input layer are components of x and y and the output layer of neuron is component of z. Training is based on the gradient method. In the network learning processes in both areas, control points are used for training and a set of check points. The check points type 1 are areas of validation and check points type 2 are the independent check points. These are used for testing and evaluating the precision interpolation networks. The error signal based on the RMSE is created and the correction of weight is used to achieve the minimum RMSE.

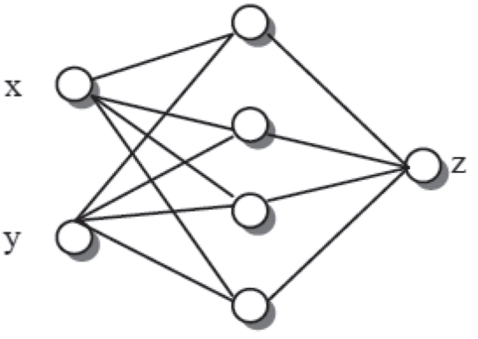

Fig. 1: Network perceptron with a hidden layer for the interpolation heights.

Tab. 1: Area Profile 1.

Elevation changes	No. of control points	No. of check points		Regional dimensions
		Type 1	Type 2	
16 m	100	45	40	250 × 275 m²

Tab. 2: Area Profile 2.

Elevation changes	No. of control points	No. of check points		Regional dimensions
		Type 1	Type 2	
6 m	50	28	28	450 × 300 m²

7 Using Genetic Algorithms in Heights Interpolation

Unlike ANN that is able to create a network for elevation interpolation, GA can only be used for the optimisation of usual methods of interpolation. The usual methods of interpolation used in this study along with GA have been optimised and are consisting of polynomials and the inverse distance weighting method, which will be described below.

7.1 *Using Genetic Algorithms in Polynomial Optimisation*

Heights of polynomials can be useful for the interpolation. The most common function to achieve this integration is the general polynomial function shown in Tab. 3 (Petrie & Kennie 1990).

It is clear that the single polynomial of a polynomial function has a special characteristic shape. Using specific terms, unique surface features can be created.

For the actual surface production in a particular model, it is not necessary to use the entire function. The operating system has the responsibility to determine what is used. Only in a few cases it is possible for the user to steer the function for modelling of the particular piece of land that is more relevant.

The first step of using of the polynomial functions is the determination of the optimal terms of these functions. The shape optimisation of the polynomials is related to the geometry and the topography of the region. GA is used to evaluate the effect of the presence or absence of various terms where the polynomial functions are used to find the most effective functions. For this purpose, a singular binary chromosome in the form of a series of zeros and ones is used. The digit zero indicates non-interference and the digit one indicates interference. In the process of GA, optimal chromosomes that show the best polynomial terms are obtained. Coefficients of the terms are determined by the least-squares method during this process. In this study, quartic polynomials are examined. For the GA optimisation, firstly the chromosomes must be formed and an initial population created. Each chromosome is made up of variables that are essentially the polynomial coefficients, which is interpreted as gene. Gene 1 represents in the desired term of polynomial and gene 0 represents the interference term in the polynomial. The first algorithm optimisation process consists of an initial population of chromosomes and the coefficients that can be calculated by control points through the least-squares method and using check points to determine the remaining residual. So by employing control points, check points and the dependent variable (RMSE), optimal chromosomes are formed. After finishing the optimisation processes, the check points, which had no interference in the optimisation process, are used to evaluate the obtained chromosomes. In other words, the process of determining proper polynomial coefficients with genetic algorithm and control points uses two types of check points. One is for the optimisation of the process under consideration of the control points to find the optimal chromosomes. They are referred to as GA check points (GACPs). The other are the independent check points used to evaluate the final chromosome, known as independent check points (ICPs). In this paper the check points type 1 and type 2 are referred to as GACPs and ICPs respectively.

Tab. 3: Polynomial function for surface reconstruction.

No. of variables	Description	Row	Equations
1	flat	zero	$z = a_0$
2	linear	first	$"flat" + a_1x + a_2y$
3	quadratic	second	$"linear" + a_3x^2 + a_4y^2 + a_5xy$
4	cubic	third	$"quadratic" + a_6x^3 + a_7y^3 + a_8x^2y + a_9xy^2$
5	quartic	fourth	$"cubic" + a_{10}x^4 + a_{11}y^4 + a_{12}x^3y + a_{13}x^2y^2 + a_{14}xy^3$

7.2 *Using Genetic Algorithms in the Optimisation of Inverse Distance Weighting Method*

GA, control and check points can be used to optimise the magnitude of strength and consequently a proper weight is achieved. In this article, from the control points and the series of check point type 1 the GACPs can be used to determine the optimised strength. Finally, the strength obtained from GA is substituted in the IDW equation and as a result, the accuracy of the algorithm with the series of check point type 2 as the independent check points through the optimisation process with GA (ICPs) are examined and evaluated. The tournament function can be used for the selection and the Gaussian function for the mutation (Eremeev 2000). The fusion function is a single-point combination for generations while 500 generations are considered in a GA process.

8 Assessment of Results

The IDW interpolation method was applied to the datasets using three different settings of the power values of the inverse distance method (Tab. 4).

Tab. 4 shows the RMSE for both datasets in the unit metre. The minimal errors can be observed with a power value of one and three in the first dataset, and three in the second dataset. Area 2 is comparably flat which explains that the best fit is found at the highest power

Tab. 4: Results obtained from IDW method.

Inverse distance power	RMSE for area 1 (m)		RMSE for area 2 (m)	
	Check points type 1	Check points type 2	Check points type 1	Check points type 2
1	1.601	1.895	0.849	1.115
2	2.130	2.375	0.744	1.005
2	1.661	1.865	0.684	0.931

Tab. 5: Results of the Kriging method.

Type of varygram	Type of Drift	RMSE for area 1 (m)		RMSE for area 2 (m)	
		Check points type 1	Check points type 2	Check points type 1	Check points type 2
Spherical	No drift	4.409	4.656	0.938	1.201
	Linear drift	2.061	2.392	0.638	0.850
	Quadratic drift	1.264	1.391	0.888	1.148
Exponential	No drift	4.409	4.656	0.939	1.203
	Linear drift	2.061	2.392	0.638	0.849
	Quadratic drift	2.060	2.391	0.890	1.151
Linear	No drift	1.219	1.374	0.648	0.900
	Linear drift	1.261	1.383	0.652	0.886
	Quadratic drift	1.260	1.383	0.647	0.898
Gaussian	No drift	4.409	4.656	0.939	1.203
	Linear drift	2.061	2.392	0.638	0.849
	Quadratic drift	2.060	2.391	0.890	1.151

value. On the other hand area 1 has a strongly undulated terrain. High power values cause a smoothing effect to the data and are therefore not appropriate to model this type of terrain. Thus, the lower power value fosters the best fit. This shows that the selection of an optimal power value is very important for a better interpolation and GA can be useful for height interpolation by the IDW method in rough surfaces. In comparison, Kriging uses several interpolation methods for the varygrams such as spherical, linear, exponential, and Gaussian. In each case, the drift types "no drift", "linear drift" and "quadratic drift" are used. The results are compared in Tab. 5.

Tab. 5 shows that the accuracy of the Gaussian and exponential varygrams are nearly the same while the highest accuracy is achieved using a linear varygram with no drift for area 1 and exponential or Gaussian linear drift for area 2.

In spherical, exponential and Gaussian varygrams, linear and quadratic drifts are more accurate compared to no drift, but in a linear varygram no drift is more accurate. Results of other methods are shown in Tab. 6.

One of the predominant properties of the Kriging method is smoothing. Therefore, the Kriging method has a lower accuracy in regions with high elevation changes that have

Tab. 6: Results obtained from other conventional interpolation methods.

Method	RMSE for area 1 (m)		RMSE for area 2 (m)	
	Check points type 1	Check points type 2	Check points type 1	Check points type 2
Natural neighbour	1.261	1.383	0.888	1.148
Nearest neighbour	1.224	1.400	0.633	0.874
Triangulation	1.224	1.400	0.633	0.874
Quartic polynomial	2.444	2.277	0.675	0.917

Tab. 7: Results from IDW optimisation method with GA (GACP = GA check point, ICP = independent check point).

	RMSE for area 1 (m)		RMSE for area 2 (m)	
Indices optimisation	2.531		2.07	
RMSE (m)	GACP	ICP	GACP	ICP
	0.762	0.920	0.648	0.881

Tab. 8: Results of quartic polynomial optimisation with GA.

Power of polynomials	No. of variables	RMSE for area 1 (m)		RMSE for area 2 (m)	
		GACP	ICP	GACP	ICP
4	15	0.662	1.115	0.466	0.684

Tab. 9: Results of interpolation using ANN.

No. of neurons in hidden Layer	RMSE for area 1 (m)	RMSE for area 2 (m)
	Check points type 2	Check points type 2
5	0.607	0.524
10	0.566	0.488

a rough surface and sharp edges. There are many factors that affect the accuracy of the Kriging method such as the number of samples and their distance in between. In the small domain of changes, the accuracy of the Kriging method and other methods are comparable. Area 2 has a small domain of elevation changes and the accuracy of the Kriging interpolation and other methods are nearly equivalent.

In contrast to Kriging, the GA in combination with control points and check points can be adapted to the terrain type by selecting an appropriate power value for the IDW method. An independent evaluation took place by using the check points type 2. Tabs. 7 and 8 compare the results that are achieved by using GA/IDW method with the quartic polynomial optimisation.

In ANN interpolation, the control points are used for training and a series of check points type 1 for validation and for testing/evaluating. Check points type 2 are used for the perceptron network with a hidden layer of 5 neurons and 10 neurons (Saati et al. 2008, Karabork et al. 2008), considering the first period size and with momentum 0.7 Ns, the following results have been obtained.

In order to compare and evaluate the interpolation methods, the results of the current methods and AI techniques are collected from the RMSE through a series of check points type 2. The reason for this is that the AI techniques at the series of check points type 1 for the optimisation process of interpolation parameters in GA and for the network validation in ANN can be used. Therefore, to ensure that the results of the optimisation process are valid, a series of check points type 2 is used as the independent check points. Consequently, the RMSE rates obtained from the conventional interpolation methods and AI techniques are compared with a series of check points type 2, which is represented in Fig. 2 as a line graph.

Fig. 2 shows with regards to area 1 (16 m altitude) that the quartic polynomial method produces the worst results. In the second region (area 2) that is wider compared to area 1 and only has 6 m altitude, the triangulation method produces better results. Thus, due to better triangles obtained in flat regions in regards to the other region, where there are greater changes in altitude, better results are achieved.

In both regions, the Kriging method for interpolation produces better results. The results

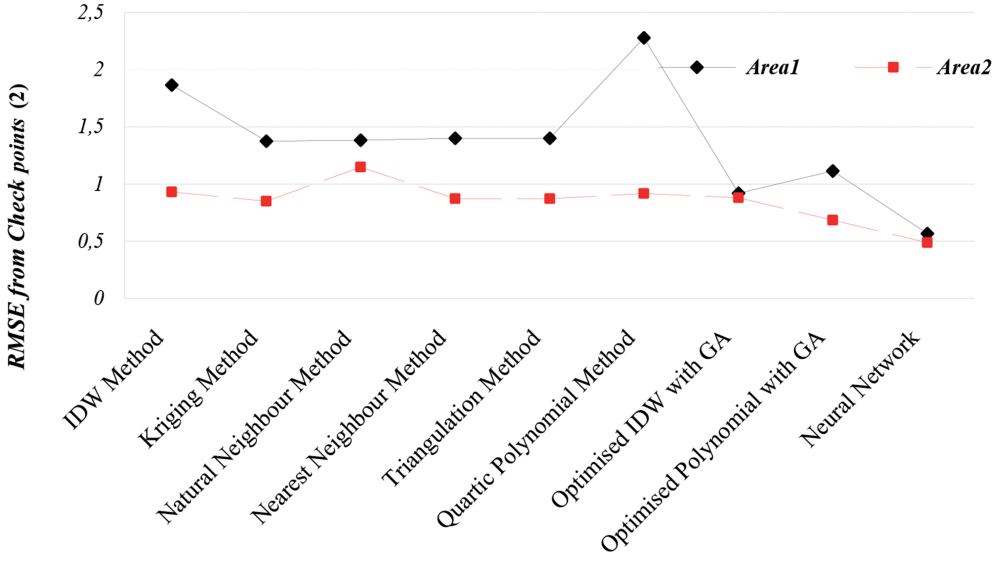

Fig. 2: Comparison of results of different interpolation methods.

of the Kriging method are very sensitive to the selection of the interpolation method of the varygram. Area 2 has a small domain of elevation changes and the accuracy of the Kriging interpolation and other methods are nearly equivalent. The Kriging method has the highest accuracy compared to other conventional methods.

In both regions, AI techniques results in a better accuracy rather than conventional methods. However, in the first region, AI techniques produce better accuracy, while the second region shows little accuracy difference with respect to conventional methods. Among the AI techniques within both regions, the best accuracy exists within ANN because it has a high ability for pattern recognition and function approximation. The quartic polynomial and the IDW that are optimised by GA have lower accuracy than ANN and better accuracy than other methods respectively for area 1 and area 2. These results show that the GA is very useful for IDW optimisation. In both areas, the IDW has a low accuracy in comparison to other conventional methods. However, with the estimation and the extraction of optimal power values and proper weight by GA, the accuracy of the optimised IDW is higher than conventional IDW. Also in area 1, the quartic polynomial has the lowest accuracy. However, by using GA and the extraction of optimal terms, the accuracy of interpolation and modelling is increasing significantly.

9 Summary and Conclusion

In the evaluation of the results, it is concluded that the use of AI techniques for height interpolation is effective and has a higher level of accuracy compared to conventional methods, especially in areas with high elevation. In order to achieve the best method for polynomial interpolation GA is used and optimal weighting parameters are achieved by the IDW method. ANN is able to determine an appropriate weight to indicate the best estimated elevation in unknown altitude regions.

Among the entire interpolation methods mentioned (conventional and intelligent), the aim is to evaluate the accuracy of interpolation methods. Universal interpolation occurs in the entire surrounding regions and as a result can be suggested for larger regions, which can be divided into smaller regions with respect to altitude changes. Within each of the smaller regions a universal interpolation can be applied. Consequently, the most important problem of distance for both conventional and intelligent interpolation methods can be solved. Also, by using universal interpolation, the time for the optimisation in GA and the training time in ANN can be reduced and thus the difficulty of applying intelligent methods in large regions with numerous sample points decreased.

References

Abdul-Rahman, A. & Pilouk, M., 2008: Spatial Data Modelling for 3D GIS. – Springer, USA.

Amidror, I., 2002: Scattered data interpolation methods for electronic imaging systems: A survey. – Journal of Electronic Imaging **11** (2): 157–176.

Chaplot, V., Darboux, F., Boureannane, H., Leguedois, S., Silvera, N. & Phachomphon, K., 2006: Accuracy of Interpolation Techniques for the Derivation of Digital Elevation Models in Relation to Landform Types and Data Density. – Geomorphology **91:** 161–172.

Eremeev, A.V., 2000: Modeling and Analysis of Genetic Algorithm with Tournament Selection. – Artificial Evolution: Lecture Notes in Computer Science **1829:** 84–95, Springer.

Eyvazi, H., Moradi, A. & Khoshgoftar, M., 2007: Optimum Determination of Interpolation Model for Using in Geographic Information Systems. – Geomatic **86**, Tehran, Iran.

Florinsky, I., 2011: Digital Terrain Analysis in Soil Science and Geology. – 1st edition, Academic Press.

Foody, G.M., McCulloch, M.B. & Yates, W.B., 1995: Classification of remotely sensed data by an artificial neural network: issues related to training data characteristics. – Photogrammetric Engineering & Remote Sensing **61** (4): 391–401.

Freisleben, B. & Merz, P., 1996: New local search operators for traveling salesman problem. – 4th International Conference on Parallel Problem Solving from Nature IV, LNCS **1141:** 22–26, Springer.

Hardy, R.L., 1971: Multiquadric equations of topography and other irregular surfaces. – Journal of Geophysical Research **76:** 1905–1915.

Hardy, R.L., 1990: Theory and applications of the multiquadric-biharmonic method. 20 years of

discovery 1968–1988. – Computers & Mathematics with Applications **19** (8–9): 163–208.

Haupt, R.L. & Haupt, S.E., 2004: Practical Genetic Algorithm. – 2nd Edition with CD, John Wiley & Sons.

Heesom, D. & Mahdjobi, L., 2001: Effect of grid resolution and terrain characteristics on data from DTM. – Journal of Computing in Civil Engineering **15** (2): 137–143.

Hertz, J., Krogh, A. & Palmer, R.G., 1991: Introduction to the Theory of Neural Computation. – Addison-Wesley, Redwood City, CA, USA.

Holland, J.H., Holyoak, K.J., Nisbett, R.E. & Thagard, P., 1989: Induction: Processes of Inference, Learning, and Discovery. – MIT Press.

Karabork, H., Baykan, O.K., Altuntas, C. & Yildz, F., 2008: Estimation of Unknown Height with Artificial Neural Network on Digital Terrain Model. – The International Archives of the Photogrammetry, Remote Sensing and Spatial Information Science **XXXVII:** 115–118.

Kasser, M. & Egels, Y., 2002: Digital Photogrammetry. – CRC Press, Boca Raton, FL, USA.

Krige, D.G., 1951: A Statistical Approach to Some Mine Valuations and Allied Problems at the Witwatersrand. – Master's thesis of the University of Witwatersrand.

Larsson, E. & Fornberg, B., 2005: Theoretical and Computational Aspects of Multivariate Interpolation with Increasingly Flat Radial Basis Functions. – Computers and Mathematics with Applications **49:** 103–130.

Li, J. & Heap, A.D., 2011: A review of comparative studies of spatial interpolation methods in environmental sciences: Performance and impact factors. – Ecological Informatics **6** (3–4): 228–241.

Li, Z., Zhu, Q. & Gold, C., 2004: Digital Terrain Modeling: Principles and Methodology. – CRC Press, Boca Raton, FL, USA.

Li, Z.L., 1990: Sampling Strategy and Accuracy Assessment for Digital Terrain Modelling. – Ph.D. thesis, University of Glasgow, UK.

Li, Z.L., 1992a: Variation of the accuracy of digital terrain models with sampling interval. – Photogrammetric Record **14** (79):113–128.

Lu, G.Y. & Wong, D.W., 2008: An adaptive inverse-distance weighting spatial interpolation technique. – Computers & Geosciences **34** (9): 1044–1055.

Mesnard, L. de, 2013: Pollution models and inverse distance weighting: Some critical remarks. – Computers & Geosciences **52:** 459–469.

Miller, C. & Laflamme, R., 1958: The digital terrain model – theory and applications. – Photogrammetric Engineering **24:** 433–442.

Mitas, L. & Mitasova, H., 1999: Spatial Interpolation, Geographic Information Systems. – Principles, techniques, management and applications: 481–492, New York, NY, USA.

Mokhtarzade, M. & Valadan Zoej, M.J., 2007: Road detection from high-resolution satellite images using artificial neural networks. – International Journal of Applied Earth Observation and Geoinformation **9:** 32–40.

Petrie, G. & Kennie, T.J.M. (eds.), 1990: Terrain Modelling in Surveying and Civil Engineering. – Whittles Publishing, Caithness, England.

Picton, P., 2000: Neural Networks. – Palgrave, Macmillan.

Ravagnani, M.A.S.S., Silva, A.P. & Constantino Arroyo, P.A., 2005: Heat exchanger network synthesis and optimisation using genetic algorithm. – Applied Thermal Engineering **25** (7): 1223–1217.

Rees, W.G., 2000: The Accuracy of Digital Elevation Models Interpolated to Higher Resolutions. – International Journal of Remote Sensing **21** (1): 7–20.

Saati, M., Amini, J. & Sadeghian, S., 2008: Generation of orthoimage from high resolution DEM and high resolution image. – Scientia Iranica **4** (4).

Sheta, A. & Turabieh, H., 2006: A comparison between genetic algorithms and sequential quadratic programming in solving constrained optimization problems. – ICGST International Journal on Artificial Intelligence and Machine Learning (AIML) **6** (1): 67–74.

Sibson, R., 1980: A Vector Identity for the Dirichlet Tesselation. – Mathematical Proceedings, Cambridge Philosophical Society **87:** 151–155.

Sibson, R., 1981: A Brief Description of Natural Neighbor Interpolation, Interpreting Multivariate Data. – Barnett, V. (ed.): John Wiley and Sons, 21–36, New York, NY, USA.

Sivanandam, S.N. & Deepa, S.N., 2010: Introduction to Genetic Algorithms. – Springer, Berlin Heidelberg.

Wagnera, P.D., Fienera, P., Wilkena, F., Kumarc., S. & Schneidera, K., 2012, Comparison and evaluation of spatial interpolation schemes for daily rainfall in data scarce regions. – Journal of Hydrology **464–465:** 388–400.

Wiszniewski, A., 1983: Accurate Fault Impedance Locating Algorithm. – IEEE Proceedings C, Generation, Transmission, Distribution **6:** 311–314.

Yanalak, M., 2003: Effect of Gridding Method on Digital Terrain Model Profile Data Based on Scattered Data. – Journal of Computing in Civil Engineering **1** (58): 58–67.

Yang, C.S., Kao, S.P., Lee, F.B. & Hung, P.S., 2004: Twelve Different Interpolation Methods: A Case Study. – ISPRS International Symposium, Istanbul, Turkey.

Zhong, D., Liu, J., Li, M. & Hao, C., 2008: NURBS reconstruction of digital terrain for hydropower engineering based on TIN model. – Progress in Natural Science **18** (11, 10): 1409–1415.

Addresses of the Authors

Hossein Bagheri & Seyyed Yousef Sadjadi, Department of Geomatics Engineering, School of Civil Engineering, University of Tafresh, Tafresh, Iran, e-mail: hosseinbagheri1366@yahoo.com, y_sadjadi@yahoo.com

Saeed Sadeghian, Geomatics College of National Cartographic Centre, Tehran, Iran , sadeghian@ncc.org.ir

Manuskript eingereicht: Dezember 2013
Angenommen: März 2014

Berichte von Veranstaltungen

13. Oldenburger 3D Tage, 12.–13. 2. 2014, Oldenburg

Die 13. Oldenburger 3D-Tage zeichneten sich auch dieses Jahr wieder durch rege Teilnahme von Vertretern von Hochschulen, Herstellern, Anwendern und Dienstleistern aus. Gegenüber dem Vorjahr konnte ein Zuwachs der Teilnehmerzahl von rund 12% auf 242 verzeichnet werden. Das überwältigende Interesse an den 50 Fachbeiträgen und der rege Austausch in den Vortragspausen bezeugte die Notwendigkeit einer solchen Veranstaltung im Lichte der rapiden Umwälzungen in Wirtschaft und Wissenschaft.

Eröffnet wurde die Veranstaltung durch Prof. Dr. Thomas Luhmann, geschäftsführender Direktor des IAPG (Institut für Angewandte Photogrammetrie und Geoinformatik) der Jade-Hochschule Oldenburg, dem Wirtschaftsminister des Landes Niedersachsen, Olaf Lies, und dem Präsident der Jade Hochschule, Dr. Elmar Schreiber. Den Eröffnungsvortrag *Automation in der 3D-Objektmodellierung – Realität oder (Alb-)Traum* von Thomas Kersten (HafenCity Universität Hamburg) zeigte, dass trotz fortschreitender Automatisierung und Entwicklung zu low-cost Systemen die Kompetenzgewalt fest in den Händen der Sachkundigen aus Photogrammetrie und Vermessung bleibt.

Im ersten Vortragsblock der Session *Deformationsanalyse* am Eröffnungstag wurden in unterschiedlichen Beiträgen Anwendungsfelder und Techniken der Deformationsanalyse aufgezeigt. Während Frank Gielsdorf von der Firma technet GmbH einen Ansatz zur Detektion von Deformationen unter Nutzung von Ebenenidentitäten vorstellte, berichtete Martina Grosse-Schwiep vom IAPG über erste Erfahrungen und Herausforderungen bei der Messung von Verformungen der Rotorblätter einer Windenergieanlage mit Laserscannern. Anschließend an die ersten beiden Vorträge referierte Boris Resnik von der Beuth Hochschule für Technik, Berlin, über Möglichkeiten zur Beobachtung der Auslenkung von Windenergieanlagen mit Tachymetern und Laserscannern im Hinblick auf die Wirtschaftlichkeit und den Nutzen. Melanie Garmann vom Geodätischen Institut der Universität Hannover rundete die Session mit einem Vortrag über das Monitoring von Brückentragwerken mittels Modellierung von Freiformkurven für Laserscanning-Profile ab.

Die parallel verlaufende Session mit dem Themenschwerpunkt *Photogrammetrie* eröffnete Heinz-Jürgen Przybilla. Verschiedenste Anwendungsgebiete bildbasierter Messsysteme und spezielle Lösungen für außergewöhnliche Problemstellungen waren Gegenstand dieser Session. Die Rekonstruktion von Freileitungsgittermasten zeigte, welche Herausforderungen photogrammetrischer Verfahren bewältigt werden müssen, um stabförmige, komplexe und große Geometrien auszuwerten. Dieser Vortrag wurde von Michael Ranzau von der Hochschule für angewandte Wissenschaften Würzburg-Schweinfurt gehalten. Der Einsatz von Photogrammetrieverfahren im Bauwesen wurde von Holger Evers von der HTWK Leipzig vorgestellt. Hier wurde zur Untersuchung des Verbundverhaltens von Beschichtungen auf Betonkörpern die Bruchfläche dreidimensional erfasst. Der Geschäftsführer von AICON, Werner Boesemann, stellte ein im Hause entwickeltes Online-Photogrammetriesystem vor. Mit diesen Systemen werden Prozesse für die Montage und Endkontrolle, z. B. von Passagiertüren und Helikopterstrukturen in der Luftfahrtindustrie, verbessert und unterstützt. Den letzten Vortrag dieser Session hielt Thomas Kersten, betitelt mit *Bildbasierte Low-Cost-Systeme zur automatischen Generierung von 3D-Modellen archäologischer Fundstücke in Äthiopien und Katar*. In der Archäologie stehen oft nicht die finanziellen Mittel für die Beschaffung von Laserscannern oder anderen kostspieligen Messwerkzeugen zur Verfügung. Bildbasierte Lösungen stellen hierbei eine kostengünstige und zudem einfach zu handhabende Alternative dar.

Ausreichend Zeit, sich über die Vorträge auszutauschen und bei einer Tasse Kaffee und belegten Schnittchen Kontakte mit Herstel-

DOI: 10.1127/1432-8364/2014/0221 1432-8364/14/0221 $ 2.75

lern und Anwendern zu pflegen, fand sich in der Pause.

Die Optimierung von bestehenden Systemkonzepten und Auswertetechniken von lichtgebenden Sensoren prägten die im Anschluss an die Mittagspause stattgefundene Vortragsreihe *Laser & Licht: Systeme*. Christian Bräuer-Burchardt vom Fraunhofer Institut für Angewandte Optik und Feinmechanik, Jena, berichtete von der direkten Phasenentfaltung durch Geometriedatennutzung bei streifenprojektionsbasierten 3D-Stereo-Sensoren. Mathias Burger vom i3mainz stellte ein Verfahren zur Registrierung von 3D-Punktwolken via 2D-Korrespondenz für ein kombiniertes Messsystem vor. Stephan Neser von der Hochschule Darmstadt präsentierte ein Konzept zur Totalkalibrierung der Entfernungsmessung einer PMD-Kamera, und die Reihe abschließend zeigte Oliver Arold (3D-Shape GmbH) ein Verfahren zur Registrierung von Aufnahmen eines handgeführten, bewegungsrobusten optischen 3D-Sensors.

Zeitgleich zur nachmittäglichen Vortragsreihe fand das erste Herstellerforum der diesjährigen Veranstaltung statt. Das von Boris Resnik (Beuth Hochschule für Technik Berlin) geleitete Herstellerforum 1 begann mit dem Vortrag *Mobile Mapping gepaart mit terrestrischen Laserscandaten* von Andreas Hermanowski (Topcon Europe). Anschließend stellte Harald Saeger Lasercanning-Lösungen von Leica Geosystems vor und ging dabei näher auf das Pegasus:One System und die Scanstation P20 ein. Ellen Klingelhöffer (Trimble AB Schweden) präsentierte den Multi-Kamera-Rover Trimble V10 mit Schwerpunkt auf dem photogrammetrischen Messsystem. Thomas Gaisecker (RIEGL LMS GmbH) zeigte die 1-Klick-Anwendung RiSOLVE und als besonderes Highlight eine APP für das iPad, die das Visualisieren und Navigieren in 3D Punktwolken ermöglicht. Abgeschlossen wurde das Forum durch Alexander Bauer (FARO Europe GmbH), der mit FARO FOCUS 3D das perfekte Werkzeug für 3D-Dokumentation und Landvermessung präsentierte.

Den Abschluss des Tages bildeten die simultan verlaufenden Sessions *3D-Dokumentation in der Archäologie und Denkmalpflege* und *Navigation und Tracking*. Erstere wurde durch den Beitrag *Verknüpfung von Punktwolken aus SFM-Verfahren mit den Daten terrestrischer Laserscanner* von Jost-Michael Broser von der FH Köln eröffnet. Die folgenden Beiträge *Fortlaufende semantische 3D-Kartierung von archäologischen Ausgrabungsstätten* von Dorit Borrmann (Julius-Maximilians-Universität Würzburg), *Anwendung des Surphaser HX25 in der Denkmalpflege* von Markus Steffen (Landesamt für Denkmalpflege Baden-Württemberg) und *Multi Method Mixture* von Thomas Schramm (HafenCity Universität Hamburg) zeigten deutlich die Wichtigkeit aktueller Auswertetechniken wie Structure-from-Motion und Laserscanning und deren Anwendungen zur 3D-Dokumentation im archäologischen Kontext.

In der letzten Session *Navigation & Tracking* des ersten Veranstaltungstages zeigten sich vor allem die fachlichen Stärken der Abteilung Geoinformation der Jade Hochschule, die hier den Großteil der Themen abdeckte. Timo Krüger von Metronom Mainz stellte ein elektromagnetisches Trackingsystem für die Anwendung in der Wirbelsäulenchirurgie vor. Das System trägt dazu bei, die bisher hohe Rate von 30% Fehlstellung von Wirbelsäulenimplantaten zu bekämpfen. Ein ebenfalls medizinischer Anwendungsfall von Tracking wurde von Jana Pilinksi von der Jade Hochschule vorgetragen. Ein optisch basiertes low-cost System soll Kopf- und Zeigebewegung eines Probanden in einem Hörtest feststellen. Dieses System soll später in Arztpraxen und Spezialkliniken Einsatz finden. Von der gleichen Hochschule präsentierte Janetta Wodniok die Untersuchung eines kommerziellen Motioncapture/Trackingsystems für den Einsatz in der Film- und Spielebranche. Mit Hilfe eines Roboters wurde ein umfangreiches Messprogramm durchgeführt, das die gewünschte Anwendungsgenauigkeit bestätigte. Das Navigieren in einem virtuellen Modell via Head-Mounted-Display wurde im Rahmen eines Masterprojektes an der Jade Hochschule umgesetzt. Knut Riegel stellte ein Stereotrackingsystem vor, das die Position und Blickrichtung eines Nutzers bestimmt und damit die Bewegung in der Augmented-Reality Umgebung ermöglicht.

Am späten Nachmittag war damit der fachwissenschaftliche Teil der Veranstaltung ab-

geschlossen. Wie schon in den Vorjahren als Tradition etabliert, fand eine Abendveranstaltung mit klassischem Grünkohl und Pinkel statt. Das Highlight des abendlichen Events bildete das Akrobatenduo „Tante Luise und Herr Kurt“, die mit ihrer Darstellung für heitere Ausgelassenheit gesorgt haben.

Am letzten Tag leitete der Vortragsblock mit den parallelen Sessions *Autonome Systeme* und *Industrielle Anwendungen* die Veranstaltung ein. Zu Beginn der Reihe *Autonome Systeme* zeigte Matthias Naumann von der Universität Rostock Untersuchungen zur Eignung von Unmanned Aerial Systems für die Deformationsanalyse von Deichbauwerken. Christoph Steffen vom Landesamt für Denkmalpflege Baden-Württemberg schloss mit der Präsentation von neuen 3D-Dokumentationsverfahren in der Denkmalpflege zur Verbindung von Structure-from-Motion und Low Altitude Aerial Photography an die Vortragsreihe an. Nachfolgend zeigte Ralf Gehrke von der Fachhochschule Frankfurt am Main, wie eine photogrammetrische Dokumentation einer archäologischen Ausgrabung aus der Sicht des Nutzers zu sehen ist. Die Session abschließend stellte Thomas Willemsen von der HafenCity Universität Hamburg einen Ansatz mit Kalman Filter vor, welcher der Fusionierung von im Smartphone verbauten Sensoren zur Innenraumpositionierung dient.

Im ersten Block des zweiten Veranstaltungstages *Industrielle Anwendung* wurde gezeigt, wie Messsysteme für die praktische Anwendung konfiguriert oder neu konzipiert werden müssen. Die Fertigung von Rotorblättern für Windkraftanlagen ist zurzeit noch mit viel Handarbeit verbunden. Fehler und Abweichungen gegenüber dem CAD-Soll führen nicht nur zu Effizienzverlusten, sondern riskieren auch teure Ausfälle. Andreas Künzel von der TU Berlin stellte ein Inspektionsverfahren vor, mit dem diese Rotorblätter automatisiert geprüft werden können. Ein stark spezialisiertes Streifenprojektionssystem stellt Bernd-Michael Wolf von Brötje Automation vor. Nietverbindungen auf Flugzeugrümpfen müssen hier teilweise sogar im Mikrometerbereich überprüft werden. Ein weiteres für die Bedürfnisse der Luftfahrtindustrie maßgefertigtes Streifenprojektionssystem wurde von Jan Burke vorgestellt. Hier liegt der Fokus vor allem auf Oberflächenqualität von Flügel- und Tragflächen. Großflächige Aufnahmen mit hoher Tiefenauflösung sind Alleinstellungsmerkmale dieses Systems. Verschiedene modulare Vielpunktsensoren für den Einsatz in der Industriemesstechnik zur Qualitätsprüfung von Bauteilen stellte Thorben Weng von Werth Messtechnik vor. Der Einsatzbereich sowie die Grenzen und Möglichkeiten dieser Sensoren wurden in diesem Vortrag dargelegt. Zum Abschluss der Session stellten zwei Studenten der Fachhochschule Mainz, Jens Wambach und Martin Lux, die von ihnen im Rahmen eines Masterprojektes entwickelte open source Software OpenIndy vor. Die Software stellt einen via Plug-Ins erweiterbaren Rahmen für Industriemesssysteme zur freien Verfügung.

Auch die zweistündige Mittagspause des zweiten Veranstaltungstages wurde für den lebhaften Austausch der Fachleute, Anwender und Hersteller genutzt. Die darauf folgende Session bot auch an diesem Tag erneut die Möglichkeit, sich über neue Hard- und Softwareentwicklungen zu informieren. Ralf Lichtenberger (LIMESS GmbH) eröffnete das Herstellerforum 2 – geleitet durch Thomas Schramm (HafenCity Universität Hamburg) – mit der Präsentation des Surphaser, einem 3D-Laserscanner der Extraklasse. Anschließend stellte Cornelius König (Ingenieurbüro Dr. König) Scalypso vor, eine Software zur Auswertung von 3D-Laserscandaten. Ulrich Clauss (Dr. Clauß Bild- und Datentechnik GmbH) erläuterte die Erzeugung virtueller 3D-Modelle auf der Grundlage kombinierter Laser- und Fotoscans. Mit dem Vortrag *Adaptive Projektion – Intelligente Beleuchtung für die 3D-Digitalisierung* beendete Thomas Mayer von Steinbichler Optotechnik GmbH das Herstellerforum.

Die immer neuen Herausforderungen an die optische 3D-Messtechnik waren Thema der Session *Laser & Licht: Korrespondenz und Oberfläche*. Christian Bräuer-Burchardt vom Fraunhofer Institut für Angewandte Optik und Feinmechanik stellte in seinem Beitrag ein System zur Hochgeschwindigkeits-Oberflächenerfassung mittels eines streifenprojektionsbasierten 3D-Sensors vor. Malte Lenoch von der TU Dortmund zeigte in einem quantitativen Vergleich verschiedene bidirek-

tionale Reflektionsverteilungsfunktionen und deren Einfluss auf die 3D-Oberflächenrekonstruktion auf. Das Hauptaugenmerk der von Marcus Grosse (Friedrich-Schiller-Universität Jena) vorgestellten Bewertungsfunktionen zur Lösung des Korrespondenzproblems über zeitliche Intensitätssequenzen liegt auf der sehr genauen optischen dreidimensionalen Vermessung, die etwa 1000 Messungen pro Sekunde ermöglicht. Abgeschlossen wurde die Session durch den Beitrag *Wirkprinzip und Funktionsweise eines 3D-Wärmescanners* von Ernst Wiedenmann (AiMESS Services GmbH).

Der letzte Vortragsblock der Oldenburger 3D-Tage befasste sich unter anderem mit *Anwendungen des Laserscannings* und verdeutlichte das breite Spektrum an Einsatzmöglichkeiten. Julia Ganitševa von der FH Mainz präsentierte in ihrem Beitrag einen Ausblick auf die vollständige und hochauflösende Erfassung von Gebäuden basierend auf Laserscanning-Technologien, welche Ausgangspunkt für den Einsatz im Feld der *Spatial Humanities* darstellt. Weitere Anwendungsfälle wurden von Ramona Baran (AirborneHydroMapping GmbH) in dem Beitrag *Die hydraulische Modellierung von Wildbächen mit Hilfe hochaufgelöster hydrographischer LiDAR-Daten*, Sven Jany (Milan Geoservice GmbH) mit *Erfassung von bergmännischen Schichten mittels TLS am Beispiel 700 m – Schacht Fulda-Neuhof* und Cristina Romero Calvo (HafenCity Universität Hamburg) mit *Schadensdokumentation der alten Schleuse am Nord-Ostsee-Kanal in Kiel* vorgestellt.

Punktwolkenverarbeitung und Interpretation war ebenfalls Thema des letzten Vortragsblocks. Wie letztlich aus generierten 3D-Daten verwertbare höherwertige Information gewonnen werden kann, war in dieser Vortragsreihe Diskussionsgegenstand. Jana Siebenbrodt stellte eine Softwarelösung der Firma kubit GmbH vor, mit der ein Beitrag zur Interpretation und Modellierung von Punktwolken für Gebäude geleistet wird. Der Lebenszyklus eines Gebäudes wird über diese Software in einem BIM-System (Building Information Model) abgebildet, um Konsistenz und Redundanzfreiheit zu gewährleisten. Die Anfertigung von Sonderlösungen für komplexe Automatisierungsaufgaben der Firma Syperion GmbH wurde an einem Anwendungsbeispiel im Tagebau von Frank Elandaloussi vorgestellt. Die von Laserscannern generierten 3D-Datensätze werden prozessiert, um Störungen wie Staub, Schmutz und Baufahrzeugverkehr herauszufiltern. Von der Leibniz Universität Hannover hat Corinna Harmening ein Forschungsprojekt zur Entwicklung eines Mess- und Auswertesystem vorgestellt, mit dem Pflanzen räumlich und zeitlich erfasst werden. Zur Phänotypisierung werden Blätter einer Pflanze durch Segmentierung erkannt und über die Zeit beobachtet. Wie zwei autonome Roboter mit dem Austausch semantischer und geometrischer Daten über ein Geoinformationssystem kooperieren, wurde von Thomas Wiemann von der Universität Osnabrück vorgetragen. Die Zusammenführung von Geometrie und Topologie in einem GIS ermöglicht die Planung komplexer Roboteraufgaben.

Den Abschluss fanden die Oldenburger 3D-Tage durch lobende Worte von Thomas Luhmann für den reibungslosen Ablauf, insbesondere gerichtet an die Mitorganisatorin Christina Müller.

Songül Polat, Burkhard Tietz,
Mathias Burger, Martin Lux,
Jens Wambach, Benedikt Rauls,
Fachhochschule Mainz

Hochschulnachrichten

Karlsruher Institut für Technologie

Dissertation von Fadwa Alshawaf

Mrs. M.Sc. Fadwa Alshawaf completed her doctorate (Dr.-Ing.) at the faculty of Civil Engineering, Geo and Environmental Sciences of the Karlsruhe Institute of Technology (KIT) on November 19th, 2013, with the work *Constructing water vapor maps by fusing InSAR, GNSS and WRF data*.

1. Reviewer: Prof. Dr.-Ing. habil. Stefan Hinz, KIT
2. Reviewer: Prof. Dr.-Ing. habil. Dr. h.c. Bernhard Heck, KIT
3. Reviewer: Prof. Dr.-Ing. Franz J. Meyer, University of Alaska Fairbanks, USA

Summary:
Temporal and spatial variations of the time delay caused due to the propagation through the atmosphere is a significant error source for microwave signals transmitted from spaceborne sensors. Phase distortions caused by atmospheric water vapor are the main limitation for the accuracy of surface deformation and topography maps derived using Interferometric Synthetic Aperture Radar (InSAR). However, if these distortions are successfully isolated from other phase contributions, InSAR can be used as a continuous data source for meteorological studies. The first objective of this work aims at combining water vapor observations from Persistent Scatterer InSAR (PSI) and Global Navigation Satellite Systems (GNSS) to derive maps of the total content of the water vapor in the atmosphere at a high spatial resolution. The second objective is to apply spatial statistical data fusion of water vapor maps from remote sensing data (PSI + GNSS) and those from numerical weather models to generate complete and more accurate maps of water vapor.

The intrinsic difference between PSI and GNSS is that PSI measures water vapor differences in time and space, while GNSS can produce estimates of the total content of water vapor in the atmosphere. We present a new method to combine the complementary properties of PSI and GNSS observations to build maps of the absolute water vapor content at the spatial density of PSI data. By building interferograms and applying PSI, the homogeneous component of water vapor is most likely eliminated. This includes a component that is correlated with the surface elevation and a linear trend that models the long wavelength variations. The elevation-dependent component is modeled based on the observations available at the sparse GNSS sites distributed within the SAR image. This model is used to calculate a value for this component at each persistent scatterer location. The elevation-dependent signal is subtracted from the GNSS observations and the residuals are analyzed to estimate the long wavelength component. The heterogeneous component, which is highly dependent of the weather conditions, is extracted from the InSAR interferograms. These three components are superimposed to build the total water vapor content.

In order to validate the water vapor maps derived using our method, we used reference maps provided by the sensor MERIS (MEdium Resolution Imaging Spectrometer), which are available simultaneous to the SAR data. The results show strong spatial correlation between the water vapor maps observed by MERIS and those derived using our method with RMS values less than 0.9 mm. Also, we evaluated the spatial structure of the water vapor maps by calculating the structure functions and power spectral densities. The structure functions show that the water vapor signal decorrelates in space at rates between 2/3 and 5/3, while the power spectral densities fall at a slope of -8/3, which agrees with the theoretical expectations.

In regions of low coherence such as forests or water surfaces, it is difficult to indentify persistent scatterers using conventional PSI techniques. Since water vapor is correlated in space, we applied the kriging technique that uses the covariance matrices of the input data to generate continuous grids of water vapor. For the purpose of improving the quality of the output water vapor maps, we applied the

method of kriging too, to fuse water vapor maps derived from PSI and GNSS with those provided by the numerical weather models. These maps are simulated by the Weather Research and Forecasting Modeling System (WRF), which produces continuous grids of atmospheric water vapor at a coarser spatial resolution and a limited accuracy. Fusing water vapor maps from the remote sensing data and those from the model provides a complete knowledge of water vapor. We performed spatial statistical data fusion based on the method of Fixed-Rank Kriging (FRK) to address the problems of high computational complexity for massive datasets and to account for different spatial resolutions of the input datasets. The covariance model associated with the FRK method constructs full covariance matrices for the input data without making assumptions of isotropy and stationarity. Using FRK makes the computational burden linear with the number of data samples.

The results show that the water vapor maps derived by data fusion have a better spatial correlation and smaller RMS values to the maps from MERIS compared to those maps derived from single datasets. In regions of low persistent scatterers density, the map of the fusion is more affected by the data from the model, while in the other regions, the fusion map is driven by the remote sensing observations.

The dissertation is available under: http://digbib.ubka.uni-karlsruhe.de/volltexte/1000038846

Dissertation von Christoph Ehrler

Mr. Dipl.-Geoinf. Christoph Ehrler completed his doctorate (Dr.-Ing.) at the faculty of Civil Engineering, Geo and Environmental Sciences of the Karlsruhe Institute of Technology (KIT) on February 13th, 2014, with the work *Scale-Wavelength Decomposition of Hyperspectral Signals – Use for Mineral Classification and Quantification*.

1. Reviewer: Prof. Dr.-Ing. habil. Stefan Hinz, KIT
2. Reviewer: apl. Prof. Dr. rer.nat. Thomas Neumann, KIT

Summary:
The research of this thesis aims at the spatial mapping of minerals based on hyperspectral data. The practical background of this work refers to intense lignite mining at the demonstration site Sokolov leading to several environmental problems. One is acid mine drainage (AMD), the acidification of soils and waters due to sulphide mineral weathering and mobilisation of heavy metals. Mineral mapping candidates were limited by climate, geology and available data to the weathering stable goethite as indicator for potentially AMD affected sites, siderite as fast neutralising carbonate, kaolinite as slowly reacting acidity buffer and quartz as inert mineral not participating in buffering reactions.

Data acquisition encompassed a hyperspectral airborne survey in the reflective (HyMap) and a multispectral survey in the thermal (AHS) domains, coupled with spectroscopic reference measurements and laboratory analysis of collected samples.

Reproducible classification and quantification require a standardised and quality controlled preprocessing, a robust parameterization of spectral absorptions and a validation of all processing. Pre-processing of the thermal domain data lacked an in-flight calibration step. A generic module adaptable to any multi- or hyperspectral thermal sensor was developed. The skin temperatures of the calibration targets are estimated from the imagery, hence relieving field teams from measuring temperature during sensor overflight. The target's spectral emissivity is typically more stable and for several materials pre-known. Adaptation of the thermal atmospheric model and destriping in summary resolved the issue of noisy and strongly deviating emissivity spectra. The thermal data was brought to a similar pre-processing quality as is standard for the reflective data. It allowed its use for quantification. Quantitative mineral fractions were derived from the samples' elemental oxide concentrations by use of the normative model NORMA, adapted to the Sokolov site.

The feature based quantitative analysis allowed to link reflective and thermal domain through validation of the map products. Overlaying spectral absorption features in mixtures can result in very complex spectral sig-

natures. Classical spectral feature analysis methods are based on simple geometric primitives like triangles or on few feature describing parameters. Lots of information is lost during feature parameterization. A multi-scale analysis of spectra at several levels-of-detail and more versatile feature describing parameters would be beneficial.

This can be realised by the continuous wavelet transform (CWT). It linearly decomposes a spectrum in frequency components (scales). Noise is separated into the smallest scale. Narrow absorptions are emphasised in small to medium scales. Wide absorptions and continuum appear in high scales. CWT can be interpreted as cross-correlation of the spectrum with the wavelet, or as multi-scale derivative of the smoothed spectrum. The Second Derivative of Gaussian mother wavelet was used as its shape is similar to a generalised absorption feature. The transform is the scaled second derivative of the Gaussian filter smoothed spectrum. Maxima and minima in the spectra leave extrema in the transform, inflection points form zero crossings. The development of these transform features over the scales characterises the shape of the absorption feature and its spectral neighbourhood. Effects of noise, illumination, moisture, grain size, viewing geometry, additive offsets and linear bias are normalised or separated in specific scales. The thesis develops two spectral analysis methods on this multi-scale decomposition.

The Wavelet Transform Feature Analysis is a quantification method. It traces related transform features over the scales and chains them into vectors. The vectors convey information about the inducing spectral feature. A versatile parameterization is possible by length, curvature, wavelength and transform amplitude development of the vectors. This drives a multivariate feature based quantification, shown to be a generalisation of the classical Spectral Feature Analysis and Spectral Derivative Analysis. This approach exploits the multi-scale decomposition of the input signal with its benefits of selective accentuation of spectral components, suppression of noise, normalisation of the input signal and selective focus on varying levels of spectral detail and neighbourhood. No previous knowledge of shape and location of characteristic features and no methodological differentiation between reflectance or emissivity nor absorption minima or maxima are required. Complex spectral shapes can be conveyed into the regression as no geometric primitives are needed for the approximation of signal structures.

On the other side, the Wavelet Coherence Mapper is a classification method. It makes use of wavelet coherence, a localised spectral similarity measure which returns a whole similarity spectrum instead of an aggregated value. Together with the multiple wavelet scales, it allows to interrogate the unknown spectrum at selectable wavelength and level of spectral detail. The local similarity around a specific narrow absorption up to the general similarity of the whole spectral continuum shape can be compared. The wavelet coherence is independent of multiplicative factors and amplitude differences. It is very sensitive to curvature direction differences, less to curvature strength. Pronounced deep absorptions are equally weighted as subtle shallow absorptions and it is invariant to inter-class amplitude differences. These features are beneficial for identification of possibly weak features within signatures of mineral mixtures. Classification of siderite, goethite and clay minerals as well as quantification of goethite and kaolinite from the hyperspectral reflective data were facilitated by the wavelet based methods and normative modelling. Derived mineral distribution patterns were plausible and followed the expectations. To complement and validate the reflective domain results, a band-ratio based quantification of kaolinite and quartz was performed on the multispectral thermal data.

Validation showed a general agreement of the distribution patterns and relative abundance trends between reflective and thermal domain for areas matching the mineralogic assemblage of the training data, albeit an offset existed. Limited transferability of the reflective domain quantitative kaolinite model was apparent for coal-clay mixtures. Pre-processing was successful. Normalised image, field and laboratory spectra matched well. Deviations in amplitude and spectral contrast of the not normalised spectra were partially compensated by the normalising character of

CWT. The influence on the quantitative models hence was small.

Future research aspects are border effects in the CWT. Masking of possibly affected bands led to classification errors at higher scales. Fast filter-bank implementations of CWT can reduce processing times and the change to a spline biorthogonal wavelet can confine the border effects. Future availability of hyperspectral airborne sensors (HySpex, TASI, SEBASS) and satellite missions (EnMAP, HyspIRI) with largely varying spatial and spectral resolution will rise issues of spectral mixing and be a promising testbed for the developed methods.

Neuerscheinung

Kohlstock, P., 2013: *Kartographie*. – 3. Auflage, Schöningh-Verlag, 237 Seiten. ISBN 978-3-8252-4064-6.

Peter Kohlstock legt mit diesem Buch eine auf langjähriger Lehrerfahrung basierende Einführung in die Kartographie vor, ausgehend von der Abbildung der Erdoberfläche über die Landesaufnahme, die Kartengestaltung und -herstellung bis zur Kartennutzung. Die insbesondere auch durch zahlreiche, zum Teil farbige Abbildungen sehr anschauliche Darstellung vermittelt die wesentlichen Grundlagen dieses für alle geowissenschaftlichen Studiengänge so wichtigen Fachgebietes als Basis für eine sachverständige Verwendung von Karten unterschiedlichster Form als Informationsquelle und Arbeitsmittel.

Das Buch ist Jörg Albertz gewidmet.

Veranstaltungskalender

2014

14.–16. Mai: **ISPRS Technical Commission IV Symposium 2014** in **Suzhou,** China. isprs.org/2014tc4symposium

19.–21. Mai: **ISPRS Technical Commission VI Symposium 2014** in **Wuhan,** China. lmars.whu.edu.cn/isprscom6

3.–5. Juni: **European Conference on Synthetic Aperture Radar (EUSAR) 2014** in **Berlin**. eusar.de

16.–21. Juni: **25. International FIG Congress 2014** in **Kuala Lumpur,** Malaysia. fig.net/fig2014

17.–19. Juni: **Computer Vision and Pattern Recognition (CVPR) 2014** in **Columbus,** USA. pamitc.org/cvpr14

23.–25. Juni: **ISPRS Technical Commission V Symposium 2014** in **Riva,** Italien. isprs-commission5.fbk.eu

13.–18. Juli: **International Geosience and Remote Sensing Symposium (IGARSS) 2014** in **Québec City,** Kanada. igarss2014.com

24.–28. August: **International Conference on Pattern Recognition (ICPR) 2014** in **Stockholm,** Schweden. icpr2014.org

5.–7. September: **ISPRS Technical Commission III Symposium – Photogrammetric Computer Vision 2014** in **Zürich,** Schweiz. isprs.org/pcv2014

5.–12. September: **European Conference on Computer Vision (ECCV) 2014** in **Zürich,** Schweiz. eccv2014.org

17.–18. September: **14. Seminar GIS & Internet** in **München**. unibw.de/inf4/professuren/geoinformatik/seminar-gis-und-internet

29. September – 2. Oktober: **ISPRS Technical Commission VII Symposium 2014** in **Istanbul,** Türkei.

6.–8. Oktober: **ISPRS Technical Commission II Symposium 2014** in **Toronto,** Kanada.

27.–30. Oktober: **International Conference on Image Processing (ICIP) 2014** in **Paris,** Frankreich. icip2014.com

17.–20. November: **ISPRS Technical Commission I Symposium 2014** in **Denver,** USA.

9.–12. Dezember: **ISPRS Technical Commission VIII Symposium 2014** in **Hyderabad,** Indien.

Weitere Konferenzen und Workshops finden sich beispielsweise unter:
isprs.org/calendar/
iris.usc.edu/Information/Iris-Conferences.html

Korporative Mitglieder

Firmen

AEROWEST GmbH
AICON 3D Systems GmbH
aphos Leipzig AG
Becker GeoInfo GmbH
Bernhard Harzer Verlag GmbH
Blom Deutschland GmbH
Brockmann Consult GmbH
bsf swissphoto GmbH
Büro Immekus
CGI Systems GmbH
DB Netz AG
DELPHI IMM GmbH
Deutsches Bergbau-Museum
EFTAS Fernerkundung Technologietransfer GmbH
ESG Elektroniksystem- und Logistik-GmbH
Esri Deutschland GmbH
EUROPEAN SPACE IMAGING
Eurosense GmbH
fokus GmbH
g.on experience gmbh
GAF GmbH
GeoCart Herten GmbH
GeoContent GmbH
Geoinform. & Photogr. Engin. Dr. Kruck & Co. GbR
geoplana Ingenieurgesellschaft mbH
GEOSYSTEMS GmbH
GGS - Büro für Geotechnik, Geoinformatik, Service
Hansa Luftbild AG
IGI - Ingenieur-Gesellschaft für Interfaces mbH
ILV Ingenieurbüro für Luftbildauswertung und Vermessung
Infoterra GmbH
INVERS - Industrievermessung & Systeme
ITT Visual Information Solutions Germany
J. Linsinger ZT-GmbH
Leica Geosystems GmbH
Luftbilddatenbank-Würzburg
Messbildstelle GmbH
Microsoft Photogrammetry
MILAN Geoservice GmbH
M.O.S.S. Computer Grafik Systeme GmbH
PHOENICS GmbH
PMS - Photo Mess Systeme AG
RapidEye AG
RIEGL Laser Measurement Systems GmbH
RWE Power AG, Geobasisdaten/Markscheidewesen
technet GmbH
topometric GmbH
TRIGIS Vermessung + Geoinformatik GmbH
Trimble Germany GmbH
trimetric 3D Service GmbH
Wichmann, VDE Verlag GmbH
Z/I Imaging Ltd.

Behörden

Amt für Geoinformationswesen der Bundeswehr
Bayerische Landesanstalt für Wald und Forstwirtschaft
Bundesamt für Kartographie und Geodäsie
Bundesmininisterium für Ernährung, Landwirtschaft und Verbraucherschutz
Hessisches LA für Bodenmanagement und Geoinformation

Innenministerium NRW, Gruppe Vermessungswesen
Institut für Umwelt- und Zukunftsforschung
LA für Geoinformation und Landentwicklung, BW
LA für Vermessung und Geoinformation, Bayern
LB Geoinformation und Vermessung, Hamburg
LB für Küstenschutz, Nationalpark und Meeresschutz, SH
Landeshauptstadt Düsseldorf, Vermessungs- und Liegenschaftsamt
Landesvermessung und Geobasisinformation Niedersachsen
Märkischer Kreis, Vermessungs- und Katasteramt
Regierungspräsident Tübingen, Abt. 8 Forstdirektion
Regionalverband Ruhr
Staatsbetrieb Sachsenforst Pirna
Stadt Bocholt, Fachbereich 31
Stadt Köln, Amt für Liegenschaften, Vermessung und Kataster
Stadt Wuppertal, Vermessung, Katasteramt und Geodaten
Thüringer LA für Vermessung und Geoinformation

Hochschulen

BTU Cottbus, Lehrstuhl für Vermessungskunde
FH Frankfurt a.M., FB 1, Studiengang Geoinformation
FH Mainz, Institut für Raumbezogene Informations- und Messtechnik
Jade Hochschule, Institut für Angewandte Photogrammetrie und Geoinformatik
HCU HafenCity Universität Hamburg, Geomatik
HfT Stuttgart, Vermessung und Geoinformatik
HS Bochum, FB Vermessung und Geoinformatik
HS Karlsruhe, Fakultät für Geomatik
HTW Dresden, FB Vermessungswesen/Kartographie
LUH Hannover, Institut für Kartographie und Geoinformatik
LUH Hannover, Institut für Photogrammetrie und Geoinformation
MLU Halle, FG Geofernerkundung
Ruhr-Uni Bochum, Geographisches Institut
RWTH Aachen, Geodätisches Institut
TU Bergak. Freiberg, Institut für Markscheidewesen und Geodäsie
TU Berlin, Computer Vision & Remote Sensing
TU Berlin, Institut für Geodäsie und Geoinformationstechnik
TU Braunschweig, Institut für Geodäsie und Photogr.
TU Clausthal, Institut für Geotechnik und Markscheidewesen
TU Darmstadt, Institut für Photogrammetrie und Kartographie
TU Dresden, Institut für Photogrammetrie und Fernerkundung
TU München, FG Photogrammetrie und Fernerkundung
TU Wien, Institut für Photogrammetrie und Fernerkundung
Uni Bonn, Institut für Photogrammetrie
Uni Göttingen, Institut für Waldinventur und Waldwachstum
Uni Heidelberg, IWR Interdisziplinäres Zentrum für Wissenschaftliches Rechnen
Uni Kassel, FB Ökologische Agrarwissenschaften
Uni Kiel, Geographisches Institut
Uni Stuttgart, Institut für Photogrammetrie
Uni Würzburg, Geographisches Institut
Uni zu Köln, Geographisches Institut

Umstellung des Einzugsverfahrens von DGPF-Mitgliedsbeiträgen auf SEPA

Zum 1. 2. 2014 hat die DGPF auf das europaweit einheitliche Zahlverfahren SEPA (**S**ingle **E**uro **P**ayments **A**rea) umgestellt, mit dem das bisherige inländische Zahlverfahren abgelöst wird.

Sie brauchen sich als Mitglied – sofern Sie bisher das Lastschrift-Einzugsverfahren für Ihren jährlichen DGPF-Mitgliedsbeitrag genutzt haben – um die Abwicklung dieser Zahlung nicht weiter zu kümmern. Ihre bereits erteilte Einzugsermächtigung wird von uns als sogenanntes *SEPA-Lastschriftmandat* weiter genutzt.

Ihre bisherigen Kontodaten, Kontonummer und Bankleitzahl, werden bei den Lastschriften durch die sogenannte *IBAN* abgelöst. Diese IBAN lässt sich automatisch aus Ihren bisherigen Kontodaten ableiten. Auf Ihrem Kontoauszug finden Sie künftig nach Abbuchung des DGPF-Mitgliedsbeitrags Ihre *Mandatsreferenznummer* und unsere von der Bundesbank vergebene *Gläubiger-Identifikationsnummer*

DE54 ZZZ0 0000 8351 37

Die Gläubiger-Identifikationsnummer der DGPF ist zu Ihrer Information sowohl auf der DGPF-Homepage als auch im Impressum der Zeitschrift PFG aufgeführt.

Für die Mandatsreferenznummer, mit der der Zahlungsvorgang dem Zahlungspflichtigen eindeutig zugeordnet werden kann, verwenden wir die Mitgliedsnummer. Sie wurde Ihnen beim Eintritt in die DGPF zugeteilt. Die Mitgliedsnummer finden Sie auf Ihrer Mitgliedskarte und auf jedem Adressaufkleber beim Versand der PFG-Hefte in der Zeile über Ihrem Namen unter **XXXX**:

*nnnn#DGPFm.**XXXX**#pppp*

Da die jährlichen Mitgliedsbeiträge nach DGPF-Satzung § 6 „bis zum Ablauf des ersten Monats“ fällig sind, werden wir sie auch künftig im Laufe der ersten drei Wochen eines Jahres einziehen.